Assessing slope uncertainties of martian Digital Elevation Models from numerical propagation of errors on synthetic geological surfaces

C. Millot, Cathy Quantin-Nataf, C. Leyrat, V. Lherm, M. Volat

Assessing slope uncertainties of martian Digital Elevation Models from numerical propagation of errors on synthetic geological surfaces

C. Millot[a], C. Quantin-Nataf[a], C. Leyrat[b], V. Lherm[a,c] and M. Volat[a]

[a]Univ Lyon, UCBL, ENSL, UJM, CNRS, LGL-TPE, F-69622, Villeurbanne, France
[b]LESIA, Observatoire de Paris, Université PSL, CNRS, Sorbonne Université, Université de Paris, 5 place Jules Janssen, 92195 Meudon, France
[c]Department of Earth and Environmental Sciences, University of Rochester, 227 Hutchison Hall, Rochester, NY 14627, USA

ARTICLE INFO

Keywords:
Mars, surface
Image processing
Instrumentation

ABSTRACT

Digital Elevation Models (DEM) are widely used in planetary sciences, including for the specific case of Mars. DEMs allow us to extract topography parameters necessary in geomorphological studies. However, DEMs are not free from vertical errors, which yields uncertainties in calculations of parameters such as local slopes. In addition, slope maps computed from DEMs often display slope patterns which are not spatially correlated with the original images. We suspect such slope patterns to originate from DEM vertical errors. To investigate this question, we propose a fully numerical method to provide a quantitative analysis of slope errors based on DEM error propagation using synthetic models. We find that the addition of vertical errors following a normal distribution (random noise) leads to the occurrence of slope patterns comparable to those in observed data. Results are similar for the two models of spatially correlated errors. We also provide estimations of slope errors for four martian cameras: HiRISE (High Resolution Imaging Science Experiment), CaSSIS (Colour and Stereo Surface Imaging System), HRSC (High Resolution Stereo Camera) and MOC (Martian Orbiter Camera). These estimations aim to be used as first order uncertainty constraints on local slopes for geomorphological studies.

1. Introduction

Digital Elevation Models (DEM) are a primary tool used to describe topographic relief on Earth and other planets such as Mars. DEMs are representations of elevation data for planetary surfaces, typically taking the form of a regular grid with the elementary element being a pixel. Each pixel has an attributed elevation value. These representations are widely used for geomorphological analysis, a major research field to characterize planetary surfaces. Three-dimensional representations and estimations of local slopes and orientations can be computed using Geographical Information System (GIS) software such as ArcGIS or QGIS. However, DEMs are not free from vertical errors on elevations. Errors can be constrained, with several studies having focused on their estimations (Heipke et al., 2007; Kirk et al., 2003, 2008; Re et al., 2019). Typically, elevation errors are not explicitly taken into account in slope calculations within GIS software, resulting in slope errors that remain unassessed. Hence, slope error computations are often restricted to standard deviation (σ) estimations of the DEM slopes under the form of a 2 or 3σ error bar. In addition, while the relationship between DEM and derived topography parameters such as slope has been extensively studied from a theoretical point of view (taking Earth's DEM as example, e.g. Heuvelink et al., 1989), slope errors on Mars' DEM are less constrained. The first modern approach to estimating error within Martian DEMs came from the work done by the Martian Orbiter Camera (MOC) from Kirk et al., 2003, with estimations of Root Mean Square (RMS) values of bidirectional slopes as a function of the DEM baseline. A number of studies then applied this method to other martian cameras (Heipke et al., 2007; Kirk et al., 2008), including High Resolution Stereo Camera (HRSC, Neukum and Jaumann, 2004) and High Resolution Imaging Science Experiment (HiRISE, McEwen et al., 2007). However, two key problems have not yet been addressed: first, the spatial structures or patterns of slope errors have not been investigated in depth. We illustrate this point with Figure 1, which highlights the correlation between HiRISE images (1B), Colour and Stereo Surface Imaging System (CaSSIS, Thomas et al., 2017) images (1C), and the resulting slope maps (respectively 1D and 1E) for two locations: Palikir Crater and Oxia Planum (1A). Spatial slope patterns are uncorrelated with geological features in the CaSSIS image (especially within the yellow square in 1C and E); moreover, high frequency slope patterns appear in the HiRISE-derived slope map 1D seemingly unrelated to the approximately homogeneous surface displayed in the HiRISE image from Figure 1B (see the blue square). Finding the source of this slope variability is important for both sites as Oxia Planum is the landing site (Quantin-Nataf et al., 2021) for the Exomars Rosalind Franklin rover, and the Palikir Crater site exhibits Recurring Slope Lineae (RSL, McEwen et al., 2011), seasonal flows of which the source mechanism remains unknown and can be linked to the angle of repose for triggering the dry mechanism hypothesis (e.g. Dundas et al., 2017, see their supplementary material, or Schmidt et al., 2017). The second problem deals with slope errors which are difficult to extract from "true" or "real" slope values (given that "true" slopes are dependent on both how they are computed and the spatial resolution of the DEM), in the sense that "true" slopes

http://eplanets.univ-lyon1.fr/?page_id=1325, cedric.millot@ens-lyon.fr (C. Millot); http://eplanets.univ-lyon1.fr/?page_id=31 (C. Quantin-Nataf); http://eplanets.univ-lyon1.fr/?page_id=1392 (M. Volat)
ORCID(s): 0000-0002-9415-7345 (C. Millot)

result from a "true" surface (i.e. free of any errors on elevations). This surface is estimated using the highest resolution DEM and is used as a reference for a given area. Such a reference is called the "ground truth" (Kirk et al., 2003). The problem is that high resolution DEMs are not free of vertical errors, even when smoothed to a coarser spatial resolution. To address these problems, we propose a complementary approach in the estimation of slope errors to investigate both issues. We first create a synthetic DEM according to different geological shapes and we add vertical errors following a normal distribution, assuming a spatial correlation between two different laws or complete independence. We then compute slopes using the Horn's method (Horn, 1981) default option in the ArcGIS 10 software on both a vertical errors-free synthetic DEM and a noisy DEM to compare resulting slope patterns. Slope errors are assessed using the following Pontius et al., 2008 method to provide laws of slope errors. Our goal is to provide complementary results to previous Mars' DEM studies (e.g. Kirk et al., 2003) by improving the understanding of DEM error propagation and slope uncertainty constraints. We aim for this paper to provide a method to simplify the interpretation of computed slope maps from a given DEM. We suggest referring to our slope uncertainty laws for the interpretation of slope map data derived from the martian DEM; this must be done after a careful review of the slope map computation method and its properties, along with a complete check for possible artifacts on the DEM. We also advise to always compare the original orbital image with the resulting slopes to compare slope patterns with local topography. Any inconsistencies between slope maps and local topographies can possibly be the result of data error propagation on slope maps.

2. Methods

We present a full numerical method based on a synthetic approach. The numerical method consists of

- creating a synthetic DEM with different shapes (tilted surfaces, craters, channels),
- computing the associated slopes using ArcGIS default equation (Horn, 1981),
- adding vertical errors to the synthetic DEM, following various laws and assumptions,
- computing the slopes from this new noisy DEM,
- comparing with the slopes from the first DEM (free of errors).

From different synthetic shapes, this method allows rapid quantification of slope errors from normally distributed input vertical errors. Each parameter is adaptable, as per the dimensions, spatial resolution or distribution of vertical errors in the DEM. The next sections detail the key steps of the method. Section 2.1 describes each synthetic shape we create, including tilted surface, simple and complex impact craters, and channels. Part 2.2 explains how we model vertical errors on the synthetic DEM and focus on their spatial distribution and the different components of errors. Section 2.3 is dedicated to the description of the default slope computation using GIS systems such as ArcGIS and QGIS. Finally, section 2.4 describes how to estimate the different components of resulting errors, involving RMS values according to the formalism detailed in Pontius et al., 2008.

2.1. Creating synthetic DEM

We aim to create synthetic DEMs providing topographies relevant for planetary surface studies. Each shape is created using a custom Matlab program. We model flat and constant sloped surfaces, craters (complex and simple crater shapes) and channels. The synthetic DEM contain 10^4 pixels (100×100) to provide robust statistics as well as low computational time, but larger DEMs are also feasible. A clockwise rotation can be easily made to modify the orientation of the DEM, as the code includes SPICE/NAIF (Spacecraft Planet Instrument C-matrix Events/Navigation and Ancillary Information Facility) libraries (Acton, 1996). It should be noted that our synthetic DEMs are schematic representations of commonly observed geological features and does not display the complexity of a real planetary surface. However, we pay attention to best respect the morphology of geological shapes as described in morphometric studies (e.g. Watters et al., 2015 for craters, Millot et al., 2021 for channels).

Synthetic constant slope We create a constant slope synthetic DEM by defining an array of elevation values z. We model this with both a constant slope θ and a pure west-facing slope (azimuth $\varphi = 270°$). θ value is set as an input and ranges from 0 (horizontal plane) to 80° (vertical plane). Each increment δz in elevation value z is computed following

$$\delta z = \tan\theta \, \delta x \,, \tag{1}$$

starting from $z = 0$ m on the left (i.e. western) column, where δx is the pixel width. The topographic profile of such simple DEM is presented Figure 2A, with a constant slope of $\theta = 30°$ with dimensionless variables.

Synthetic impact craters Craters are created using Legendre polynomials. A given crater profile is defined as

$$z(\alpha) = R\cos\alpha \tag{2}$$

where α is the angle between the vertical axis and R (see Figure 3), which is

$$R = \sum_{n=0}^{N} a_n \tilde{P}_n(\cos\alpha) \,. \tag{3}$$

$\tilde{P}_n$ are shifted Legendre polynomials of degree n and N is the highest Legendre polynomial degree. Both crater shapes

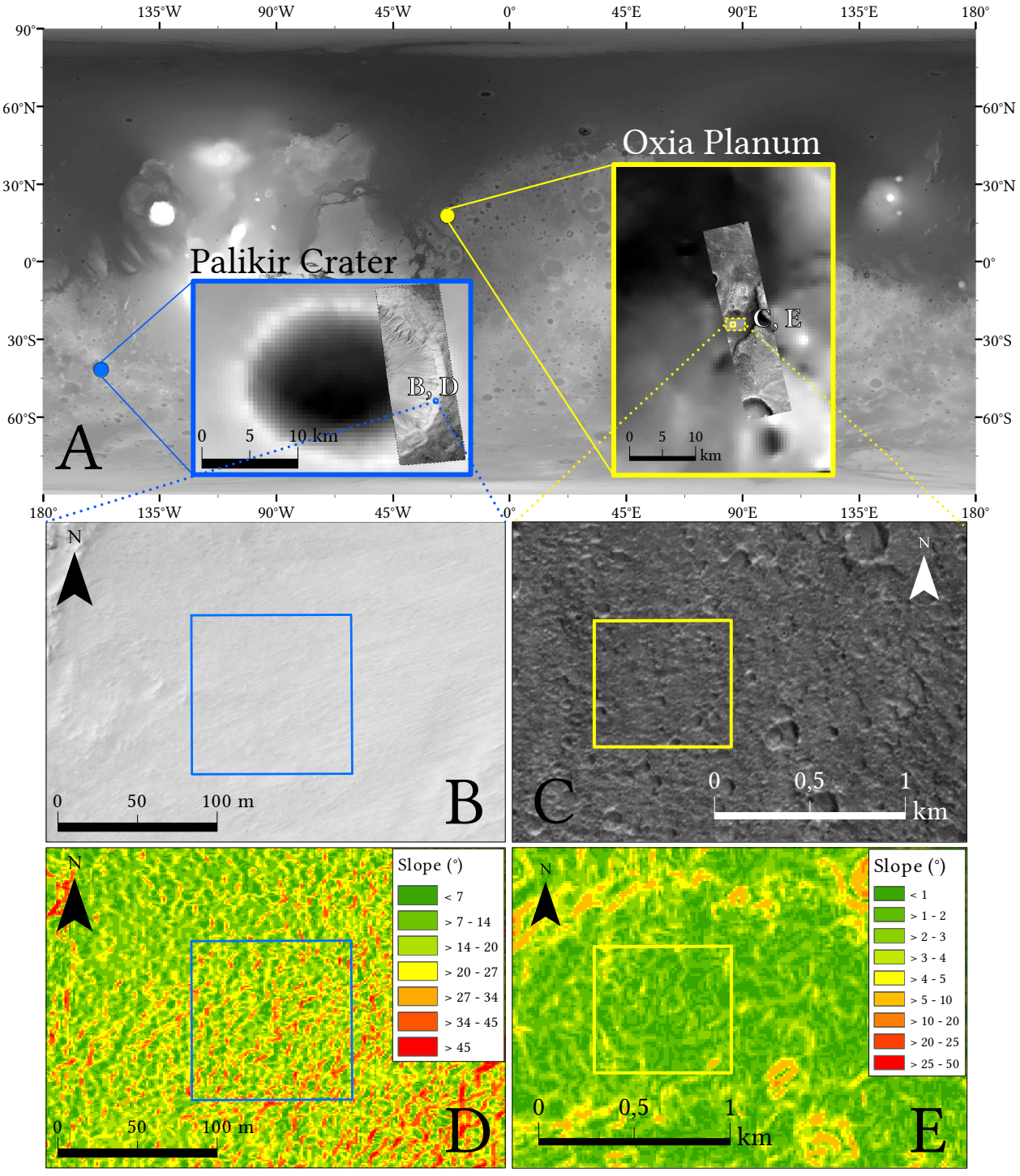

Figure 1: A) Close-up on Palikir Crater locations of respectively HiRISE DEM (Kirk et al., 2008) and CaSSIS DEM (Simioni et al., 2017) and their related orthoimages, superimposed on the global MOLA map (Smith et al., 1999) to provide a topography context. B) HiRISE orthoimage PSP_005943_1380 located in Palikir Crater (e.g. McEwen et al., 2011), used to create HiRISE DEM DTEEC_005943_1380_011428_1380 and displaying the eastern part of the crater wall. Main slope orientation is northwest. C) CaSSIS stereo image MY34_005664_163_1 used to create CaSSIS DEM DTM-MY34_005664_163_1. Yellow square is displayed to be used as a spatial reference in E. The CaSSIS DEM is located in Oxia Planum Rosalind Franklin's landing site (Quantin-Nataf et al., 2021). D) and E) Slope maps for C and D areas from 1 m/pixel HiRISE and 5 m/pixel CaSSIS DEM previously named. Slope variability is present within D, especially in the central blue square compared with quite homogeneous surface in B. Apparent noise is also visible in slope values within yellow square in E and seems to be poorly correlated with geological features in C.

are modeled until $N = 2$. Hence, simple and complex craters are defined as

$$z(\alpha) = \left[a_0\tilde{P}_0(\cos\alpha) + a_1\tilde{P}_1(\cos\alpha) + a_2\tilde{P}_2(\cos\alpha)\right]\cos\alpha\,.$$

a_n coefficients are related to morphometric equations from martian craters' studies. Morphometric equations are used in our study to create realistic crater shapes for Mars. Distinctions between simple and complex craters are made, thus, we use the following scaling law from Watters et al., 2015 for simple craters:

$$d = 0.205 \pm 0.012 D^{1.012}\,, \tag{4}$$

where d is the maximum depth and D is the diameter in km. Watters et al., 2015's study has been done at HiRISE resolution, yielding accurate measurements of morphometric parameters thanks to the high precision of the DEM (vertical precision around 0.2 px, Kirk et al., 2008). For complex craters, we use the following equation 5 from a morphometric study made using the Mars Observer Laser Altimeter (MOLA, Zuber et al., 1992) which has a global resolution of ~500 m/pixel (Smith et al., 1999). This spatial resolution is very different from HiRISE resolution, which resolves metric objects (Kirk et al., 2008; McEwen et al., 2007). For Mars, complex craters are restricted to diameters > 6-7 km (Melosh, 1989), which can be resolved by MOLA. Thus, we take the scaling law for complex craters from Robbins and Hynek, 2012, the expression of which is

$$d = 0.286 D^{0.582}\,. \tag{5}$$

We choose to use dimensionless depth $\tilde{d} = d/L$ and diameter $\tilde{D} = D/L$, using length $L = nR$ where n is the number of pixels along x and R is the resolution in m/px. Equations 4 and 5 are used to provide expressions for a_n Legendre polynomials coefficients. Coefficients a_0, a_1, a_2 for simple craters A_s and for complex craters A_c are

$$A_s = \begin{pmatrix} 0.7090 \\ -0.2840 \\ 0.0250 \end{pmatrix},\ A_c = \begin{pmatrix} 0.6299 \\ -0.2449 \\ -0.0150 \end{pmatrix}$$

for a dimensionless depth $\tilde{d} = 0.4$. Equations 4 and 5 provide the relationship between d and D, which depends on a_0 and a_1, assuming a_0 and a_1 are determined from these equations. a_2 controls central peak height, so it has been tuned with respect to the synthetic crater's profile for both simple and complex craters (following Wood, 1973), in order to obtain a smooth rounded shape for simple craters and central peak for complex craters.

Two topographic profiles derived from synthetic craters are displayed in Figure 2B: the blue solid line is the topographic profile crossing the central point (where $x = 0$) of a simple crater, while the red line represents the complex case.

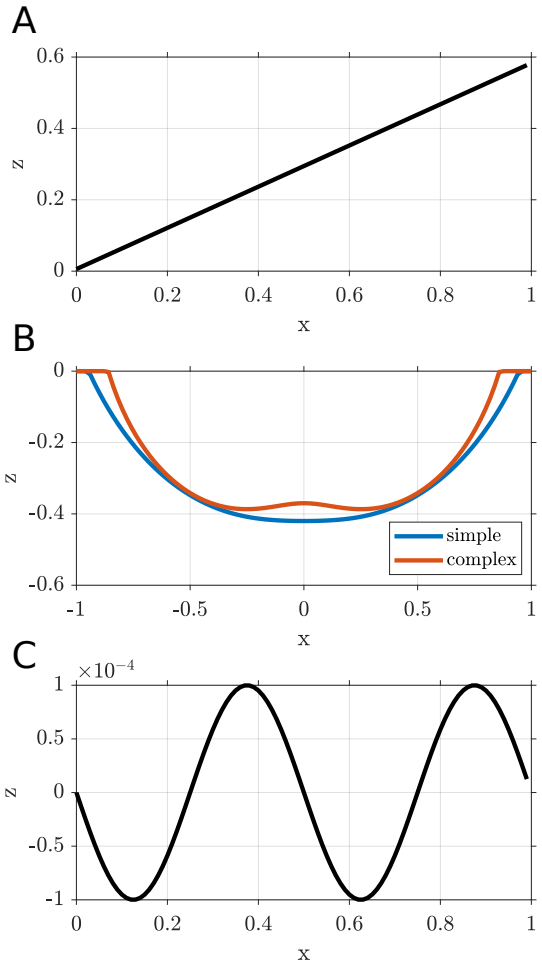

Figure 2: Topographic profiles derived from synthetic A) constant slope DEM, with a slope value $\theta = 30°$; B) simple (in blue) and complex (in red) craters DEM, with dimensionless depth $\tilde{d} = 0.4$ for the first and $\tilde{d} = 0.37$ for the second; C) channels DEM, with $\tilde{d}_c = 0.02$ and $k = 2$. x and z are dimensionless.

Notice the presence of a central peak for the complex profile. Its height is set according to complex crater morphology through the ratio of the central peak height h_{cp} and crater diameter D. We have estimated this ratio on four complex craters using MOLA data and also derived data from the topographic profile presented in Craddock et al., 1997 ("fresh" crater from their Figure 2). We find that $h_{cp}/D = 0.015 - 0.020$ for the entire dataset, so the a_2 value is defined following this constraint for the complex case.

Synthetic channels Typically, morphometric investigations focus on large scale valley networks (e.g. outflow channels, Baker and Kochel, 1978; Williams and Phillips, 2001; Ansan and Mangold, 2013), providing morphometric equations describing terrains with low topographic gradients. In order to cover a wide range of slopes, these morphometric equations are not modified. In this study, we only use morphometric parameters closer to small scale channels such as gul-

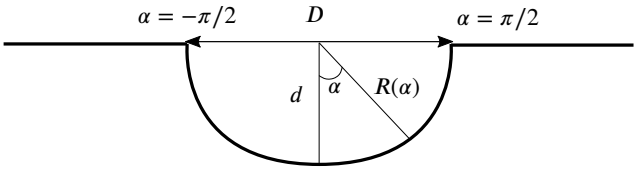

Figure 3: Schematic representation with different morphometric parameters for the synthetic crater modeled using Legendre polynomials. D is the diameter, $R(\alpha)$ is the radius and d is the maximum depth (defined for $\alpha = 0$).

lies (Malin and Edgett, 2000) and Recurring Slope Lineae (RSL, McEwen et al., 2011). In particular, RSL can be correlated with a local signal on topography as presented in Chojnacki et al., 2016 and Millot et al., 2021, providing both first order depth and spatial wavelength. Channels features are modeled using the following equation:

$$Z(x) = -\frac{1}{2}\tilde{d_c}\sin kx\,, \tag{6}$$

where k is the number of waves on the DEM for a given length L, and $\tilde{d_c} = d_c/L$ is the dimensionless channels depth. One can play with the number of channels k and their depth d_c. An example is displayed on Figure 2C, with $d_c = 0.02$ and $k = 2$.

2.2. Vertical errors

2.2.1. Random errors

We add vertical errors on the synthetic DEM to model realistic noise as expected for a "real" DEM. Theoretically, errors can be divided into two parts: one part is called the systematic error; the other part is the random error. Systematic error is a constant or predictable shift with respect to the expected value; random error is associated to the variability against the expected value for a repeated number of measurements (e.g. Taylor, 1997). Errors on measurements can be systematic or random, however most of the time the overall error is a combination of both (e.g. Ku et al., 1966). Systematic error is also known as a bias in the measurements. In the case of a DEM created by stereophotogrammetry, such a component of error can be created by jitter effects (Kirk et al., 2003, 2008; Sutton et al., 2015) of the satellite. Jitter for HiRISE camera is amplified though the motions of independent Charged Coupled Devices (CCD), which can cause misalignment between CCD seams (e.g. Sutton et al., 2015, their Figure 1). However, jitter effects tend to be minimized by correction algorithms. For this study, we assume that correction algorithm have removed jitter-associated errors in elevation. Matching errors, which are errors in matching objects between multiple images, also require manual corrections to avoid severe artefacts such as those occurring within interpolated areas (Kirk et al., 2008). We exclude manually corrected areas from our study. On a MOLA DEM, we assume there is no bias, that is, there is no systematic error, so vertical errors are only due to random error caused by the precision of the altimeter. As DEMs provided by other cameras are orthorectified on MOLA's surface, the RMS difference between the orthorectified DEM and MOLA is close to zero. Systematic error can be caused on MOLA interpolated areas, due to the lack of MOLA tracks used as a reference for images with small footprints (MOC and HiRISE). According to Sutton et al., 2022, this situation is rare for HiRISE and can be treated using CTX DEM as an intermediate ground reference (see their section 2.1.3). Hence, we also assume that systematic errors produced by an incorrect orthorectification on MOLA are negligible on HRSC (Neukum and Jaumann, 2004), MOC (Kirk et al., 2003), HiRISE (McEwen et al., 2007) and CaSSIS (Thomas et al., 2017) DEM. Vertical errors on elevation are defined following a normal distribution. Thus,

Camera	$\mathrm{d}z$	Pixel size	$\tilde{\mathrm{d}z}$	σ
HRSC	10 m	50 m	0.2	5 m
MOC	~0.22 px	~10 m	~0.22	1.1 m
HiRISE	<0.5 m	1 m	<0.5	0.25 m
CaSSIS	5 m	20 m	0.25	2.5 m

Table 1
Table summarizing camera parameters with vertical errors $\mathrm{d}z$, pixel size and dimensionless vertical errors $\tilde{\mathrm{d}z}$, following constraints from literature (HiRISE (McEwen et al., 2007; Kirk et al., 2008; Sutton et al., 2015); CaSSIS (Thomas et al., 2017; Re et al., 2019); HRSC (Neukum and Jaumann, 2004; Jaumann et al., 2007; Gwinner et al., 2009); MOC (Kirk et al., 2003)). σ is the standard deviation used to parameterize the law of vertical errors applied to synthetic DEM for each camera. σ is set as $\sigma = \mathrm{d}z/2$.

$$\mathrm{d}z \sim \mathcal{N}(\mu, \sigma^2)\,,$$

where $\mu = 0$ m and σ is defined according to the upper limit of error values $\mathrm{d}z$, following constraints provided by the literature. For our study, σ is set to half of the $\mathrm{d}z$ value, which assumes 95% of vertical errors are within $\pm\mathrm{d}z$ for a normal distribution. This value is chosen as it ensures the magnitude of vertical errors respects constraints from previous studies (e.g. Kirk et al., 2008 and see table 1); at the same time, this definition does not prevent the occurrence of larger errors, as could be the case on a single DEM. $\mathrm{d}z$ are summarized in table 1 for each Mars orbiter's camera. Expected precision may vary between different DEMs for the same camera (e.g. Sutton et al., 2015).

2.2.2. *Autocorrelated errors*

By definition, random error assumes spatial independence between each pixel of the DEM. In other words, if an element of the DEM is associated with a large vertical error, it would not impact the errors on neighboring pixels. As pointed out in several studies (e.g. Hunter and Goodchild, 1997), spatial correlation between errors is more realistic than assuming a complete independence between neighboring pixels. Hence, we use an autoregressive error model (see e.g. Le Gallo, 2000) to model the effects of spatially correlated errors. The autoregressive errors model takes the following form:

$$\mathrm{d}z_{t+1} = \rho\, \underline{W}\, \mathrm{d}z_t + \epsilon\,, \tag{7}$$

where $\mathrm{d}z_t$ are errors at time t in the form of a vector, ρ is a correlation parameter between 0 and 1, ϵ is a vector of spatially independent errors $\sim \mathcal{N}(0,1)$ and $\underline{W}$ is the weight matrix. This definition states that high errors tend to be clustered with high errors; suggesting there is a spatial correlation between errors. The two important parameters are ρ and $\underline{W}$ to define the correlation between neighboring areas. We define $\underline{W}$ according to commonly used weight matrices in econometric modeling and physical geography studies (Hunter and Goodchild, 1997; Le Gallo, 2000; McMillen, 1992). We choose to focus on two well-known studied definitions of weight matrices:

1. the contiguity matrix which gives weights to adjacent pixels. Contiguity matrix is defined as follows:

$$\begin{cases} W_{ij} = 1 & \text{for rook's} - \text{case neighbors} \\ W_{ij} = 0 & \text{otherwise} \end{cases} \tag{8}$$

2. the weight matrix following an inverse exponential distance law which sets higher coefficients to closer pixels according to this equation:

$$W_{ij} = \mathrm{e}^{-\alpha\, d_{ij}}\,, \tag{9}$$

where d_{ij} is the euclidean distance and α is a parameter defined empirically, set to $\alpha = 4$ here. The impact of α on the weights W_{ij} with different euclidean distances d_{ij} has been described in Figure 4. As α increases, weights on the reference pixel becomes higher compared to distant pixels and autocorrelation decreases. Conversely, spatial correlation is total for $\alpha = 0$.

For all our calculations, ρ is set to 0.99 to provide positive and negative errors patches efficiently, with a low number of iterations n_t. The convergence of equation 7 occurs for variable n_t, depending on the definition of $\underline{W}$. We test the convergence by running our program with multiple n_t values and test if convergence is reached for $n_t \sim 5 - 10$ for the exponential law and ~ 50 for the contiguity matrix.

2.3. Slope computations

There are multiple methods to compute slopes and several studies have pointed out their differences (Skidmore, 1989; Dunn and Hickey, 1998; Raaflaub and Collins, 2006; Tang et al., 2013). Empirically, we assess that typical planetary surface studies use GIS software to compute slopes from a DEM. The most popular GIS software applications, namely ArcGIS and QGIS, both use the definition from Horn, 1981 (see ArcGIS and QGIS documentation, both consulted on 11th February, 2021) as default options. To provide a wide range of results for the slope tool, we study their definition, which follows the equation

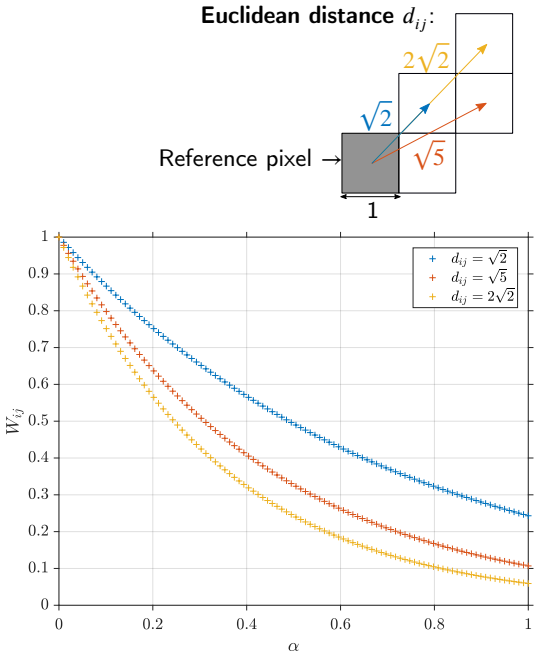

Figure 4: Impact of α value (ranging from 0 to 1) on matrix weights W_{ij} for three different euclidean distances d_{ij}. Weights are higher on closer pixels and decrease with d_{ij} for a given α. When α increases, the spatial correlation decreases as the weights imposed on neighboring pixels lowers.

$$\theta = \arctan\sqrt{\left(\frac{\partial z}{\partial x}\right)^2 + \left(\frac{\partial z}{\partial y}\right)^2} \tag{10}$$

with

$$\begin{cases} \dfrac{\partial z}{\partial x} = \dfrac{z_3 + 2z_6 + z_9 - z_1 - 2z_4 - z_7}{8\,\mathrm{d}x}\,, \\ \dfrac{\partial z}{\partial y} = \dfrac{z_7 + 2z_8 + z_9 - z_1 - 2z_2 - z_3}{8\,\mathrm{d}y}\,. \end{cases} \tag{11}$$

where θ is the local slope, z_i with $i = 1, 2, ..., 9$ are local elevations for each surrounding pixel and $\mathrm{d}x$ and $\mathrm{d}y$ are width and height, respectively, as shown in Figure 5. Pixels located closer to the central pixel have higher weighting coefficients, as illustrated by the "2" coefficient for pixel 2, 4, 6 and 8 in equation 11. Defining $\mathrm{d}x = \mathrm{d}y = 1$ coefficients vary as $2 \times (1/d^2)$, where d is the center of pixel to the center of window distance for the eight pixels surrounding the central pixel.

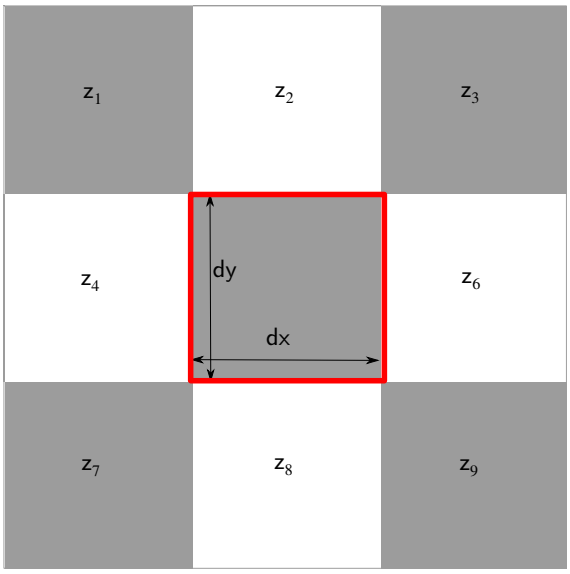

Figure 5: Representation of the 3×3 window used to compute central pixel slope (highlighted by red boundaries). Nearest pixels have higher weights.

2.4. Quantifying errors on slopes

An intuitive way to evaluate errors between two maps is to compute the pixel by pixel differences. One can take the quadratic mean (more widely known as Root Mean Square value) and standard deviation to get statistical descriptors of these differences. However, as errors between two maps have different components which are independent, we choose to follow the statistical description method of the Root Mean Square Errors (RMSE) as proposed in Pontius et al., 2008. This is used to quantify the resulting errors from noisy slope maps in order to separate the different components of errors from the pixel to pixel scale (random error) up to the whole map scale (systematic error). We calculate two error components on a $n \times m$ grid to evaluate the error following the expressions

$$\mathrm{RMS_Q} = \sqrt{\left[\frac{\sum_{i=1}^{n}\sum_{j=1}^{m}(\theta_{ij}^{s} - \theta_{ij})}{n \times m}\right]^2} \tag{12}$$

for error on quantity at map scale and

$$\mathrm{RMS_{px}} = \sqrt{\frac{\sum_{i=1}^{n}\sum_{j=1}^{m}(\theta_{ij}^{s} - \theta_{ij})^2}{n \times m}} - \mathrm{RMS_Q} \tag{13}$$

for error on pixel location (Pontius et al., 2008), where θ_{ij}^{s} and θ_{ij} are respectively synthetic and noisy slopes. The sum of $\mathrm{RMS_{px}}$ and $\mathrm{RMS_Q}$ is the total RMS error between the two maps. We will refer to RMS, $\mathrm{RMS_{px}}$ and $\mathrm{RMS_Q}$ in the results part of this study.

3. Results

In this study, we focus on only instruments collecting data yielding to Mars' DEM products: HiRISE, MOC, CaSSIS and HRSC. Additionaly, we focus on DEMs produced by stereophotogrammetry as they represent a large component of the elevation data available for Mars, thanks to the widely used SOCET SET (e.g. McEwen et al., 2007) or Ames Stereo Pipeline (ASP, e.g. Watters et al., 2015) stereopipelines. Pixel size and vertical errors $\mathrm{d}z$ are summarized in the table 1 for each instrument. We use HiRISE parameters from table 1 to create a synthetic DEM and compute the slope maps in parts 3.1 and 3.3. Synthetic slope maps are also compared to slope values derived from a real DEM (part 3.2). The spatial resolution of the synthetic DEM is 1 m/pixel and vertical errors are under 0.5 m, as specified by Kirk et al., 2008. Thus, vertical errors follow a normal law $\mathrm{d}z \sim \mathcal{N}(0, \sigma^2)$ with $\sigma = 0.25$ m. This implies that 95% of errors are under $2\sigma = 0.5$ m (see methods part 2.2). We define the same criterion of $2\sigma = \mathrm{d}z$ for other cameras to compute our general laws (part 3.4). Autoregressive definitions of vertical errors (part 3.3) from equation 7 involve heteroskedasticity, that is, a change in the errors distribution's variance (σ^2) value, so we must adapt σ to obtain slope errors distributions comparable to normal's law definition. We tune σ in order to get an output variance σ^2 for the distribution of vertical autoregressive errors equal to σ^2 for independent errors, with a difference threshold lower than 1%.

3.1. Slope maps on synthetic DEM with random errors

We compute slope maps for a range of different synthetic DEMs, from tilted or flat surfaces to crater and channels shapes. Figure 6 presents our results for a tilted surface, with a 30° slope used as input (6A and B) for a 100×100 computation grid, with a 1 m/pixel resolution. Slope aspect is west. Figure 6B presents a perfectly constant slope value of 30°. Apparent vertical banding is due to colorscale and numerical precision issues for a spatially constant value; this effect does not represent any real change in slope value. Adding noise with respect to the methods presented in section 2.2 yields to a noisy DEM (6C) and its resulting slope map (6D). Figure 6D shows how the addition of random vertical noise affects the resulting slopes following a normal law whose parameters are $\overline{\mathrm{d}z} = 0$ m and $\sigma = 0.25$ m. Significant slope variations occur, yielding to differences of up to $\pm 10 - 15°$ (6F) for maximum vertical errors of ∼75 cm (for a 1 m/pixel resolution, 6E). Intuitively, higher vertical errors provide higher slope variations. Figure 6D and F underline also the preferential orientation of the slope patterns (i.e. patches of low or high slope values) as most of them are aligned perpendicularly to the slope direction. Differences between both maps can reach $\sim 10 - 15°$ locally. We also highlight how slopes derived from flat terrains are affected by the addition of normal noise, as summarized in Figure 7. As expected, flat surfaces (7A) yield a homogeneous slope value of 0° (7B). Slope values increase heterogeneously (7C) while normal noise (7E) is added to the synthetic DEM (7D). High slope values patterns appear, with no preferred shape or orientation (7D-F), which suggests that significant slope is necessary to observe stretched slope patterns, perpendicular to

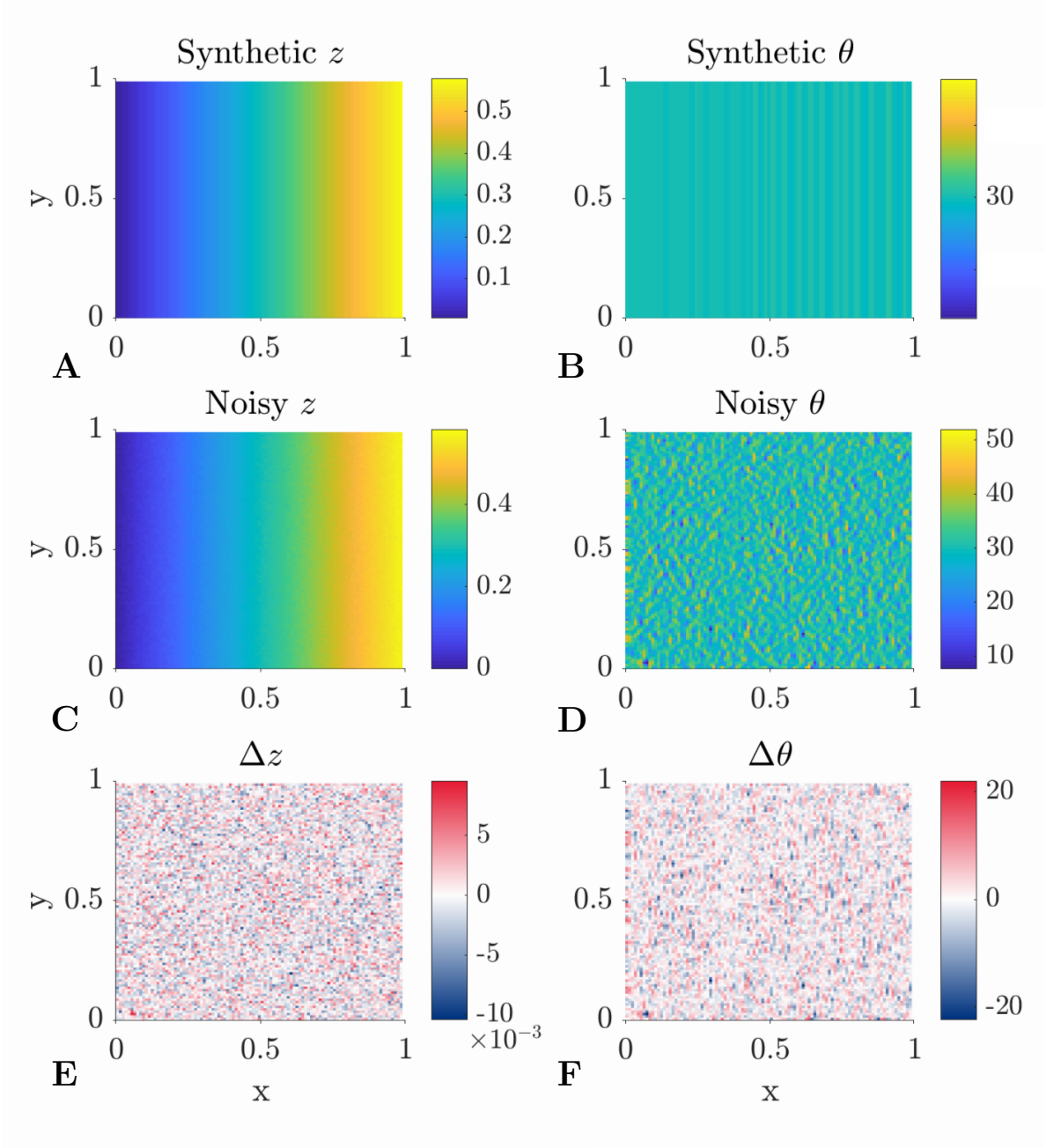

Figure 6: Results for models with a resolution of 1 m/pixel and vertical errors $\mathrm{d}z \sim \mathcal{N}(0, \sigma^2)$. A) Synthetic elevations with a 30° westward slope (if north is up). B) Slopes computed from A. C) Synthetic elevations with normally distributed noise and same slope. D) Slopes computed from C. E) Elevations differences between A and C. F) Slope differences between B and D.

the slope direction. Highest slopes are around 15° and can exceed 20° locally (7F). Crater shapes have been also investigated. Simple crater shape results are summarized in figure 8 and complex crater shape results in figure 9. Both highlight how slope patterns are oriented with respect to the centripetal direction of the slope (8F and 9F), which confirms the results for the tilted surface. The highest slope variations are underlined in Figures 8F and 9F in a form of a succession of positive/negative slope differences patterns. These high discrepancies are expected for mid-range slopes, around 30 – 40° (green and light blue areas on synthetic slope maps 8B and 9B). We also notice that central uplift for complex crater shapes (9A and B) becomes blurred in the noisy slope map 9, compared to the synthetic slope map 9. This suggests quite intuitively that small scale topographies are more impacted by DEM vertical noise than large scale topographies. Channel shapes have also been modeled and results are summarized within Figure 10. Three channels are present in the synthetic DEM (10A) which has a dimensionless depth of $\tilde{d}_c = 0.5$. The resulting synthetic slope map (10B) shows

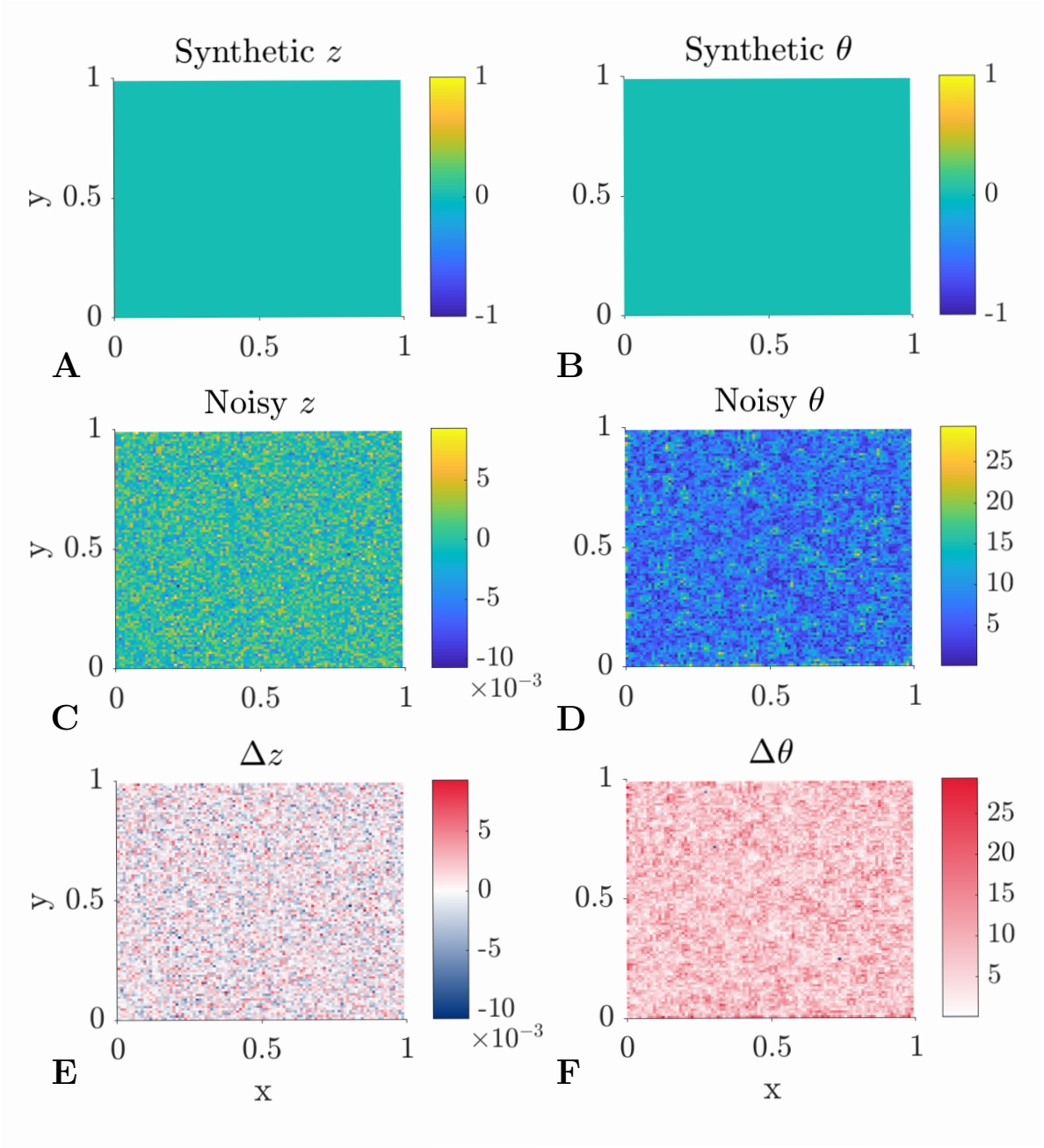

Figure 7: Results for models with a resolution of 1 m/pixel and vertical errors $\mathrm{d}z \sim \mathcal{N}(0, \sigma^2)$. A) Synthetic elevations with a flat surface. B) Slopes computed from A. C) Synthetic elevations with normally distributed noise and still a flat surface. D) Slopes computed from C. E) Elevations differences between A and C. F) Slope differences between B and D.

that values often exceed 50°, excepted on crests and valley bottoms, where the surface flattens. The main differences in slope are concentrated within these low to medium (from $\sim 0 - 40°$) slope areas (10F), which is consistent with what we find on crater shapes. Overall, Figures 8, 9 and 10 show that highest slope errors are concentrated for low to moderate slopes, assuming spatially independent vertical errors.

3.2. Comparison between synthetic and real data

Synthetic and real DEM are now compared. As an example, the area of the eastern walls of Palikir Crater has been taken from Figure 1B, using HiRISE image PSP_005943_1380 (11A). Figures 11B and 11C are elevations and slopes from the HiRISE DEM, respectively; 11D and 11E are elevations and slopes from the synthetic DEM. The synthetic DEM has been created using constraints taken from the literature for the HiRISE DEM. These are summarized in table 1. Please note the synthetic DEM in 11D has been rotated to allow a better visual comparison with the the real DEM, showing both the real and synthetic DEMs in a west-northwest slope direction (B and D). All axes from B to E are distances along

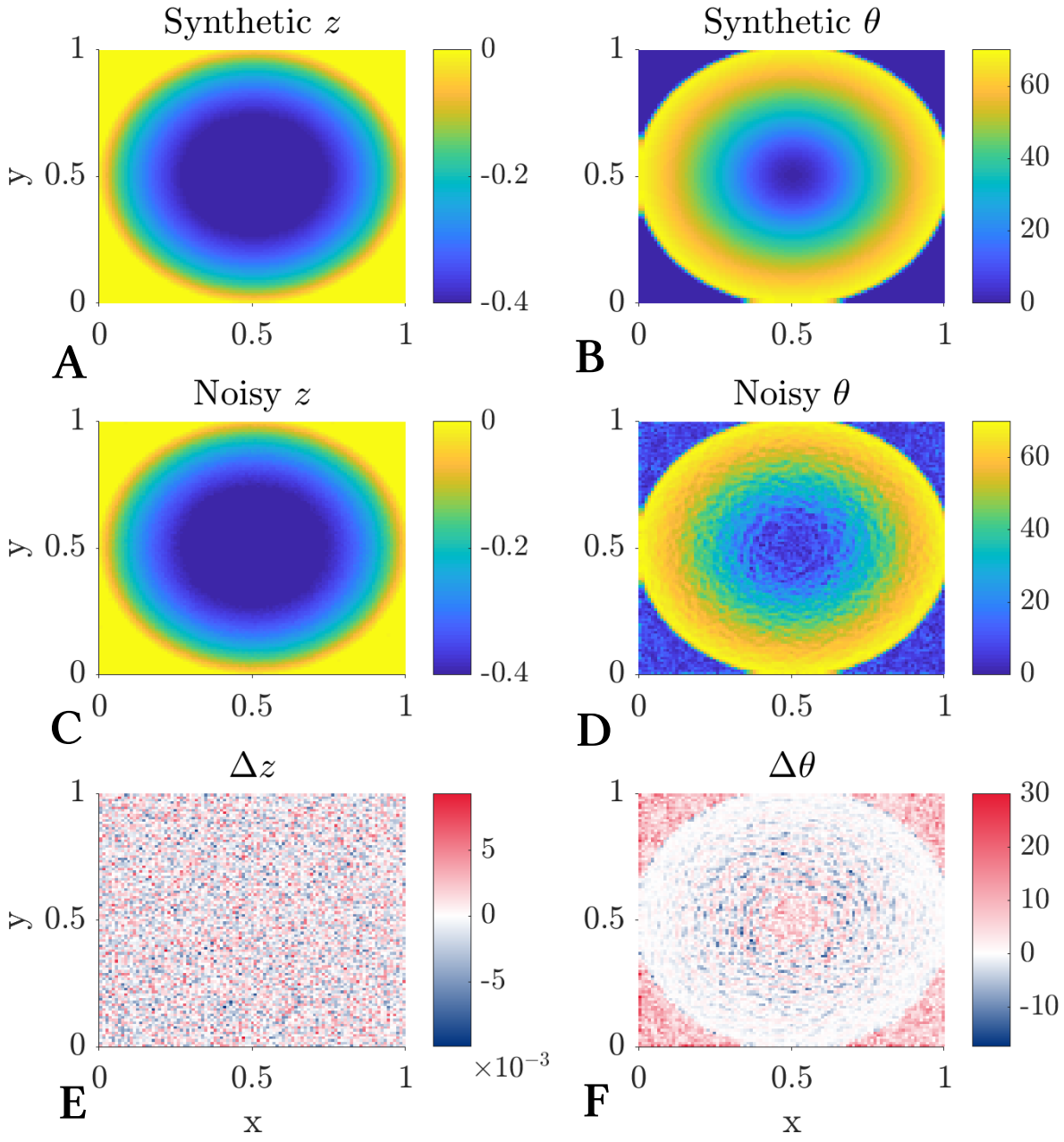

Figure 8: Results for simple crater shape models with a resolution of 1 m/pixel and vertical errors $\mathrm{d}z \sim \mathcal{N}(0, \sigma^2)$. A) Synthetic elevations with a simple crater of dimensionless depth $\tilde{d} = 0.4$. B) Slopes computed from A. C) Synthetic elevations with normally distributed noise and the same crater shape. D) Slopes computed from C. E) Elevations differences between A and C. F) Slope differences between B and D.

x and y directions. 11F is the synthetic slope map histogram; 11G is the data-derived slope map histogram. The x-axis is the slope and the y-axis is the relative number of pixels with a given slope value θ (%). Plain orange and yellow lines are normal laws sharing the same mean and standard deviation as histograms for synthetic and real data. Our results show that each output slope (C and E) presents slope patterns aligned perpendicularly to the slope direction. Our synthetic data successfully reproduces the preferential direction of slope patterns. One noticeable difference arises from the wavelength of these slope patterns: wavelength is larger for the real DEM than the synthetic one. This difference occurs for two reasons: first, the real DEM describes local topographies of several meters to several kilometers that far exceed in size the topographies created by random errors; and secondly, data are usually smoothed by a filter (e.g. a boxcar filter, see Kirk et al., 2008; a median filter and a boxcar filter in Re et al., 2019 for CaSSIS image). Finally, distributions of slope values represented in parts F and G are similar to the normal laws for both data, with the synthetic distribution in F having a slightly flattened shape. Data-derived

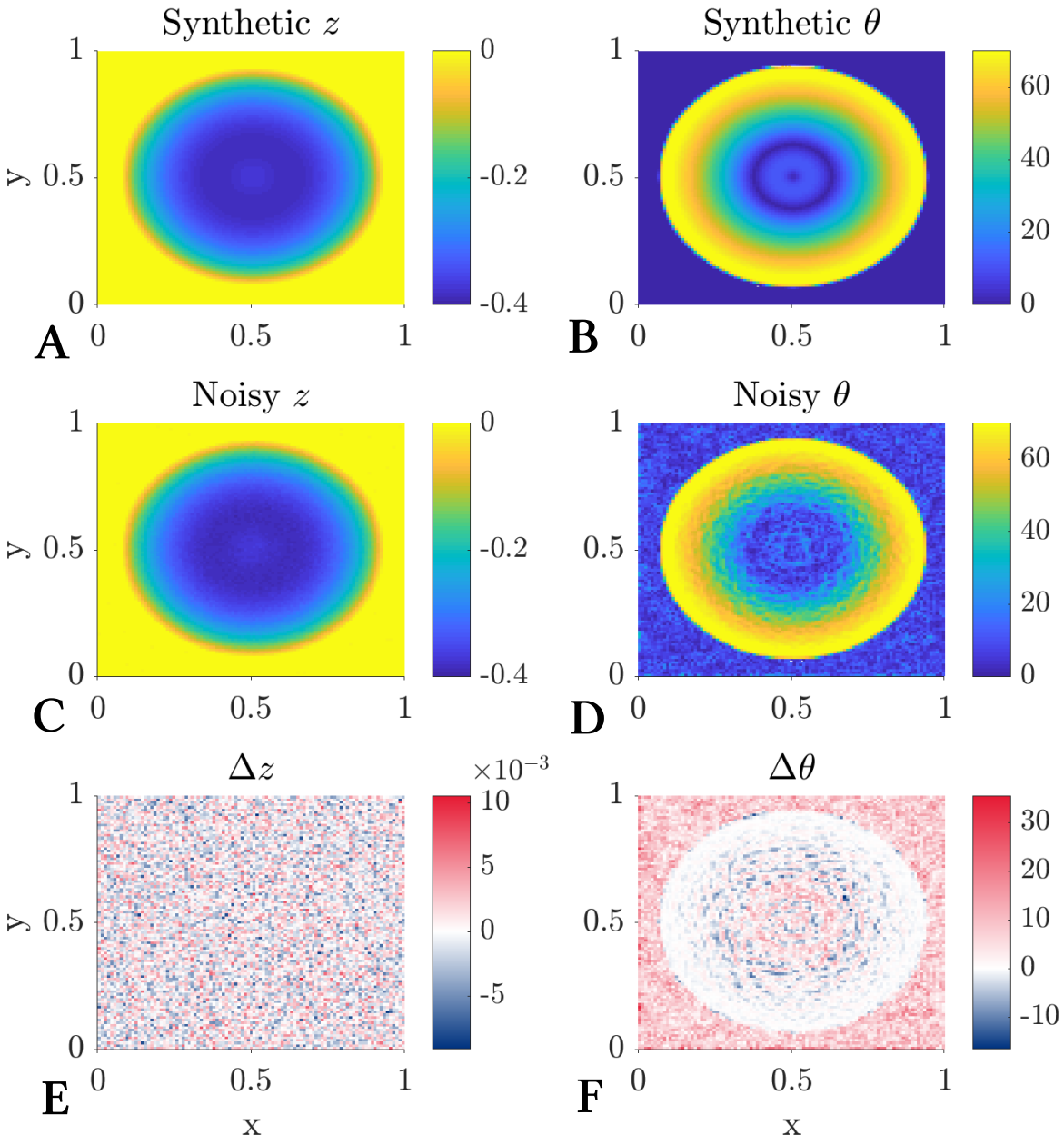

Figure 9: Results for complex crater shape models with a resolution of 1 m/pixel and vertical errors $\mathrm{d}z \sim \mathcal{N}(0, \sigma^2)$. A) Synthetic elevations with a complex crater of dimensionless depth $\tilde{d} = 0.4$. B) Slopes computed from A. C) Synthetic elevations with normally distributed noise and the same crater shape. D) Slopes computed from C. E) Elevations differences between A and C. F) Slope differences between B and D.

slopes have a mean of $\overline{\theta} = 18.7°$and a standard deviation of $\sigma_\theta = 8.6°$. Comparable values are retrieved from synthetic slopes with $\overline{\theta} = 19.1°$and $\sigma_\theta = 8.7°$. Extreme values in both distributions range from around 0°to 45-50°. To summarize, synthetic data reproduce the slope distribution of real data successfully, as well as both the occurrence and the direction of slope patterns. One limit is that synthetic data do not succeed in reproducing the correct size of slope patterns.

To provide a better textural comparison between synthetic and real slope maps, we add a smoothing filter on synthetic DEMs using CaSSIS DEM parameters and compare it with the real CaSSIS DEM. Initial synthetic DEM was completely flat before the addition of vertical noise and set to a 5 m/pixel spatial resolution. We add vertical errors following a normal lawwith a standard deviation of $\sigma = 4.0$ m. Then, the synthetic DEM is smoothed by a 3×3 gaussian filter using the default algorithm in Matlab. Figure 12 compares a smoothed synthetic CaSSIS DEM with a 3×3 gaussian filter (12A) with a small section of a real CaSSIS DEM (CAS-DTM-MY34_005664_163_1-OPD, 12B). The

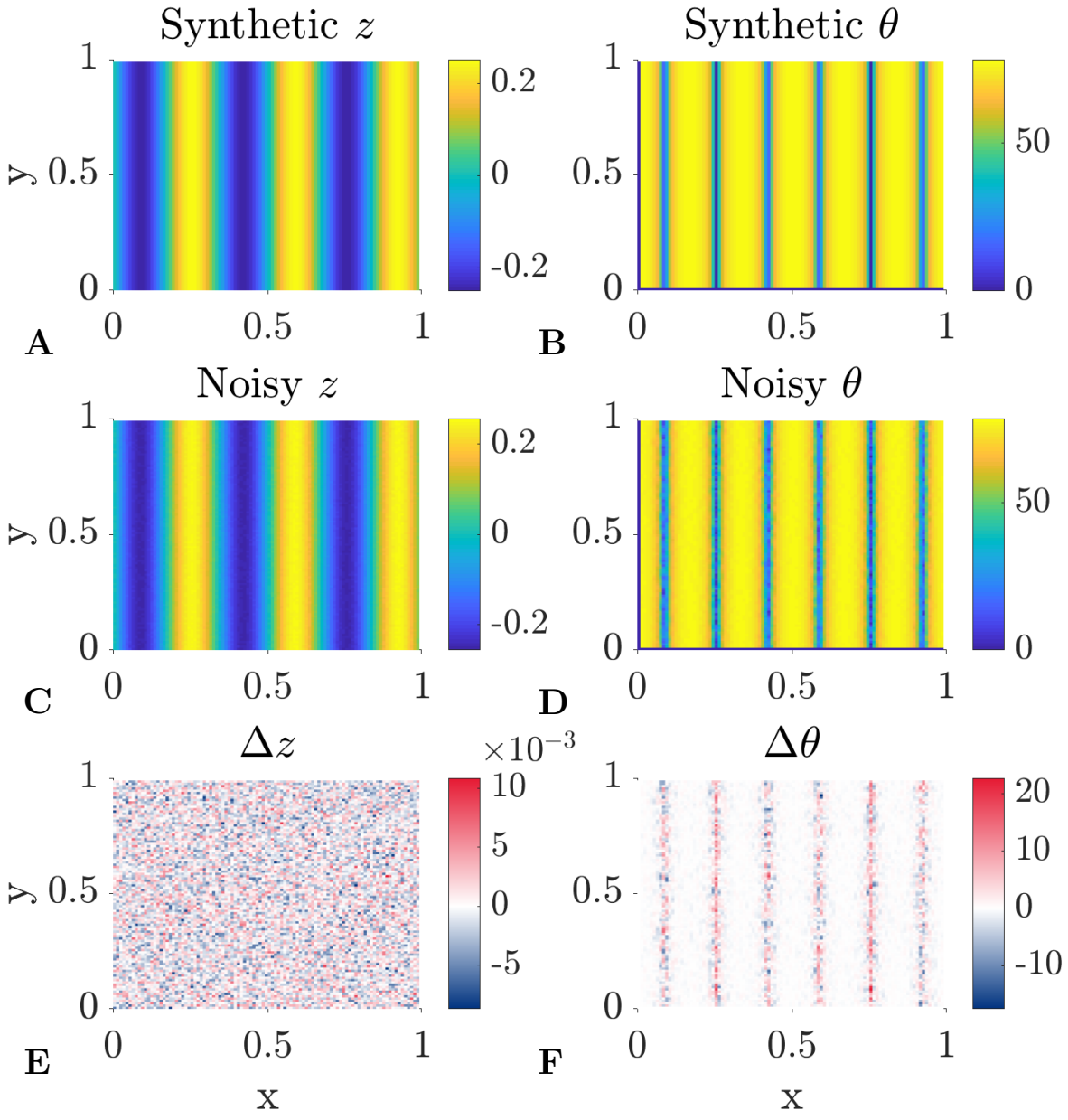

Figure 10: Results for channel shape models with a resolution of 1 m/pixel and vertical errors $dz \sim \mathcal{N}(0, \sigma^2)$. A) Synthetic elevations with 3 channels of dimensionless depth $\tilde{d}_c = 0.5$. B) Slopes computed from A. C) Synthetic elevations with normally distributed noise and the same channel shape, with parameters from A. D) Slopes computed from C. E) Elevations differences between A and C. F) Slope differences between B and D.

location of the CaSSIS data is the yellow square from Figure 1E. Slope extrema for both images are similar, and range from 0 to 5.5°. The addition of a smoothing filter yields to the occurrence of comparable slope patterns, with a typical wavelength of 3 – 5 pixels in width. Overall, the addition of a smoothing filter similar to those used in the making of the real DEM produces a better visual comparison between synthetic and real data.

3.3. Slope errors from DEM autoregressive errors

In this part, we determine the impact of autocorrelation of DEM vertical errors (equation 7) on slope values. Figures 13 and 14 present slope computations performed with two different laws of DEM vertical errors: autoregressive errors using a contiguity weight matrix for figure 13 and autoregressive errors involving an inverse exponential weight matrix for Figure 14. Both figures are built upon slope calculations performed from a 30° tilted surface with a west orientation. Figures 13A and C are dimensionless DEM ver-

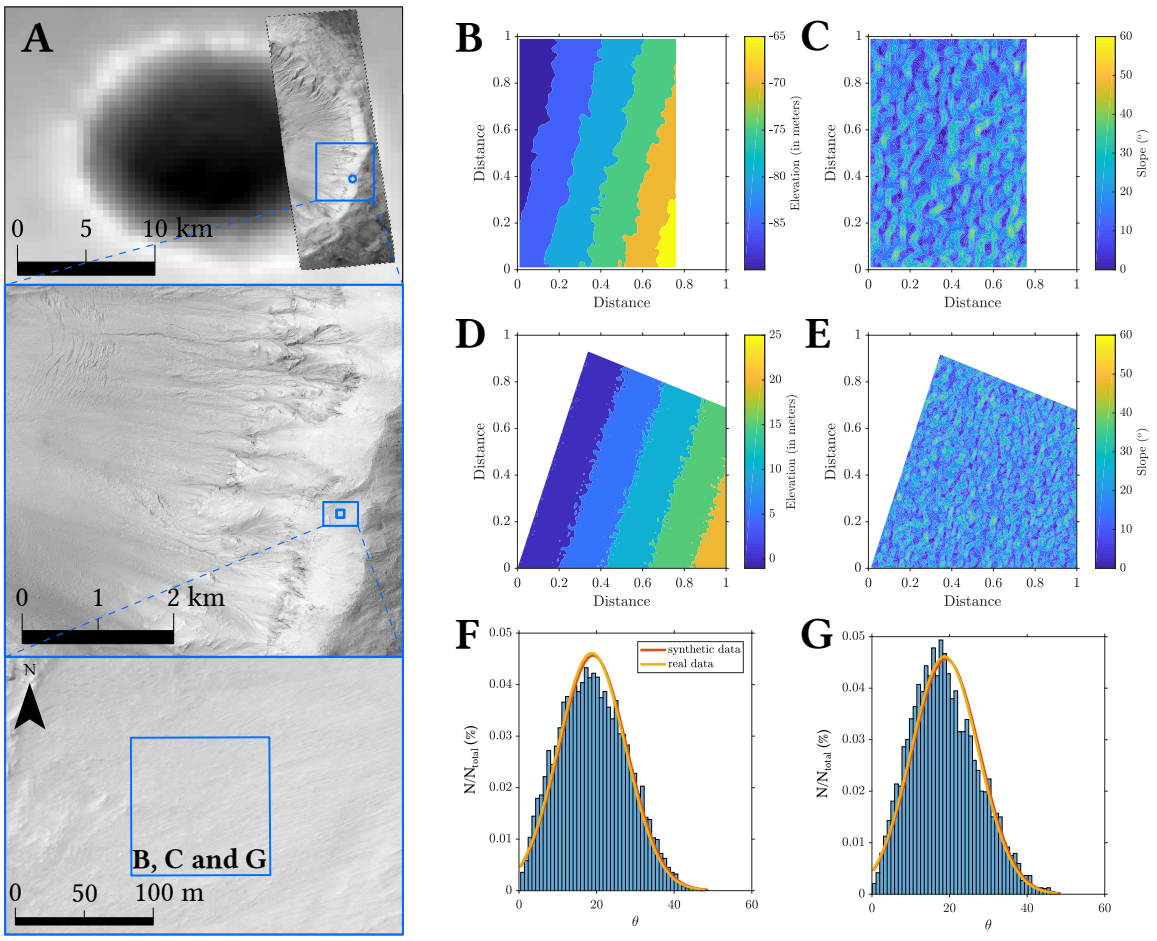

Figure 11: A) From top to bottom, successive close-up of study area, global MOLA (463 m/pixel) and HIRISE image PSP_005943_1380 (0.25 cm/pixel). The blue square is the studied region, presenting a quite homogeneous surface. B) and C) are elevations and slopes derived from HiRISE DEM DTEEC_005943_1380_011428_1380 (1 m/pixel) within the region of interest, respectively. D) and E) are synthetic elevations and slopes. Mean slope is set to fit with mean data slope and vertical uncertainties correspond to the constraints from literature (Kirk et al., 2008). F) and G) are histograms showing slope distributions for synthetic and real data, respectively. Orange and yellow plain lines are normal laws to be used as a reference, using statistical parameters from the synthetic and real data.

tical errors following equation 7 with a weight matrix $\underline{W}$ defined as a contiguity matrix (equation 8). Figure 13B is the slope map resulting from a horizontal surface with the vertical errors in 13A, and figure 13D comes from a 30° tilted DEM with the vertical errors in 13C. The distribution of vertical errors (13A and C) is quite different from previous assumptions, namely the spatial independence of errors, as patches of positive and negative errors are clearly visible due to the spatial autocorrelation of errors. Patches are often associated with what we call "checkerboard patterns" with adjacent pixels displaying successively high and low absolute values, for instance in 13C around x = 0.5 and y = 0 to 0.25 where high negative values of errors (blue pixels) are next to low values (white pixels). The autoregressive behavior does not produce significant changes in slope pattern structures. Figure 13B shows the typical random patterns already observed in Figure 7D for a noisy flat DEM, with the same global texture. The typical wavelength of the patterns do not change significantly from our results in Figure 7D as they are restricted to less than three pixels on average in the slope direction. Figure 13D highlights slope patterns similar to the ones previously reported in Figure 6D. Patches of low (in blue) and high (in yellow) slopes are preferentially aligned northward, normal to the westward slope direction. Figure 14 is similar to Figure 13, except the definition of $\underline{W}$ which follows the inverse exponential law described in equation 9. Visual analysis of Figures 14A anc C underlines that autocorrelation is less pronounced than for the contiguity law due to the absence of well-defined patches. However, negative and positive vertical errors are located within preferential areas with aggregates of blue and red pixels. Moreover, the checkerboard pattern effect previously identified for the contiguity matrix is no longer present using the exponential weight matrix. Slopes (figures 14B and D) do not differ significantly from results with spatially independent errors (figures 7D and 6D): slope patterns that are characteristic of deviations from synthetic results remain of the same wavelength and direction, that is, random patterns for the flat

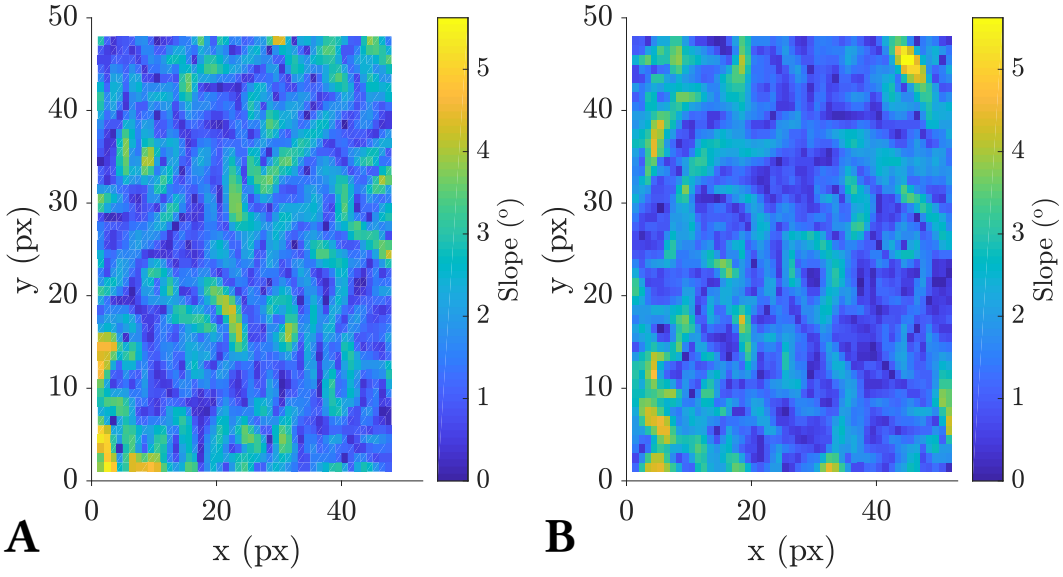

Figure 12: A) Slope map from synthetic DEM with a 3×3 gaussian filter. B) Slope map from CaSSIS DEM, from the area presented in Figure 1E.

DEM (14B) and stretched slope patterns aligned normally to the main slope direction (14D).

3.4. Precision laws for martian DEM

Now, we aim to provide an assessment of slope errors in a more quantitative way. These estimations are designed to be used as a first constraint on slope errors for studies based on topography data. Figure 15 shows the different components of the total slope error for the synthetic DEM with HiRISE parameters (spatial resolution of 1 m/pixel, $\sigma = 0.25$ m, see table 1). Again, we assume that vertical errors dz are spatially independent. Each bar is created from RMS component calculations (equations 12 and 13) using one slope map computation on a noisy tilted synthetic DEM. We obtain the total RMS for a synthetic DEM's input slope ranging from 0 to 80°, with adaptive steps of 2° between 0 and 10°, steps of 5° between 10 and 50° and steps of 10° between 50 and 80°: this involves seventeen slope map computations based on the synthetic DEM to obtain the results. Figure 15 represents a stacked bar plot, with orange bars representing RMS_Q component (equation 12) and blue bars representing RMS_{px} component (equation 13). Examples are displayed for an initial slope of 0° and 30° to describe how RMS values are related to visible slope patterns. For low input slope values, we can see that RMS_Q is the main source of errors, as its contribution reaches almost 90% of the total error for 0°. The top-left illustration in Figure 15 emphasizes that the mean value of output slopes is significantly higher (around 7.3° with this set of parameters) than the input slope $\theta = 0°$. As input slope increases, the part of RMS_Q decreases: its contribution is around 5% around 30° of input slope. RMS_Q becomes negligible when input slope exceeds 40°. Hence, RMS_Q provides information about how different the mean value of a map is from our expectations. On the right part of the Figure 15, the slope map for an input slope of 30° is represented. The mean slope value is approximately the same between synthetic and noisy slope maps, with a difference of less than 0.2°. The main component of errors come from pixel by pixel slope variations, which is the RMS_{px} value. RMS_{px} is visible in the succession of red to blue/blue to red slope difference patterns along the slope direction. For slopes higher than 60°, RMS values significantly decrease to become negligible for subvertical surfaces. However, this effect may not be representative of real data, as DEM errors can be higher in steep slope areas, especially for DEMs produced by stereophotogrammetry. We will discuss this in more detail in part 4. We now estimate the impact of different martian orbiter's cameras using vertical accuracy assessments and spatial resolution of their DEM products from literature as summarized in table 1. Results are presented in Figure 16 under the form of cumulative histograms like the example from Figure 15. Each histogram is an average result from a thousand computations, with a 3σ bars to show the computations variability. Note that the vertical scale varies for each camera. To better compare the magnitude of the uncertainties laws, we advise the reader to refer to the figure 17. Each line shows results for particular camera parameters (table 1): from top to bottom, HiRISE (16A, B and C), CaSSIS (16D, E and F), MOC (16G, H and I) and HRSC (16J, K and L). Each column represents one law of errors, namely independence (16A, D, G and J), autoregression using contiguity matrix (16B, E, H and K) and autoregression using inverse exponential matrix (16C, F, I and L). HiRISE is the camera displaying the highest RMS values with respect to other cameras, reaching at least RMS $\sim 8°$ for a 0° DEM input slope including spatial autocorrelation (16B and

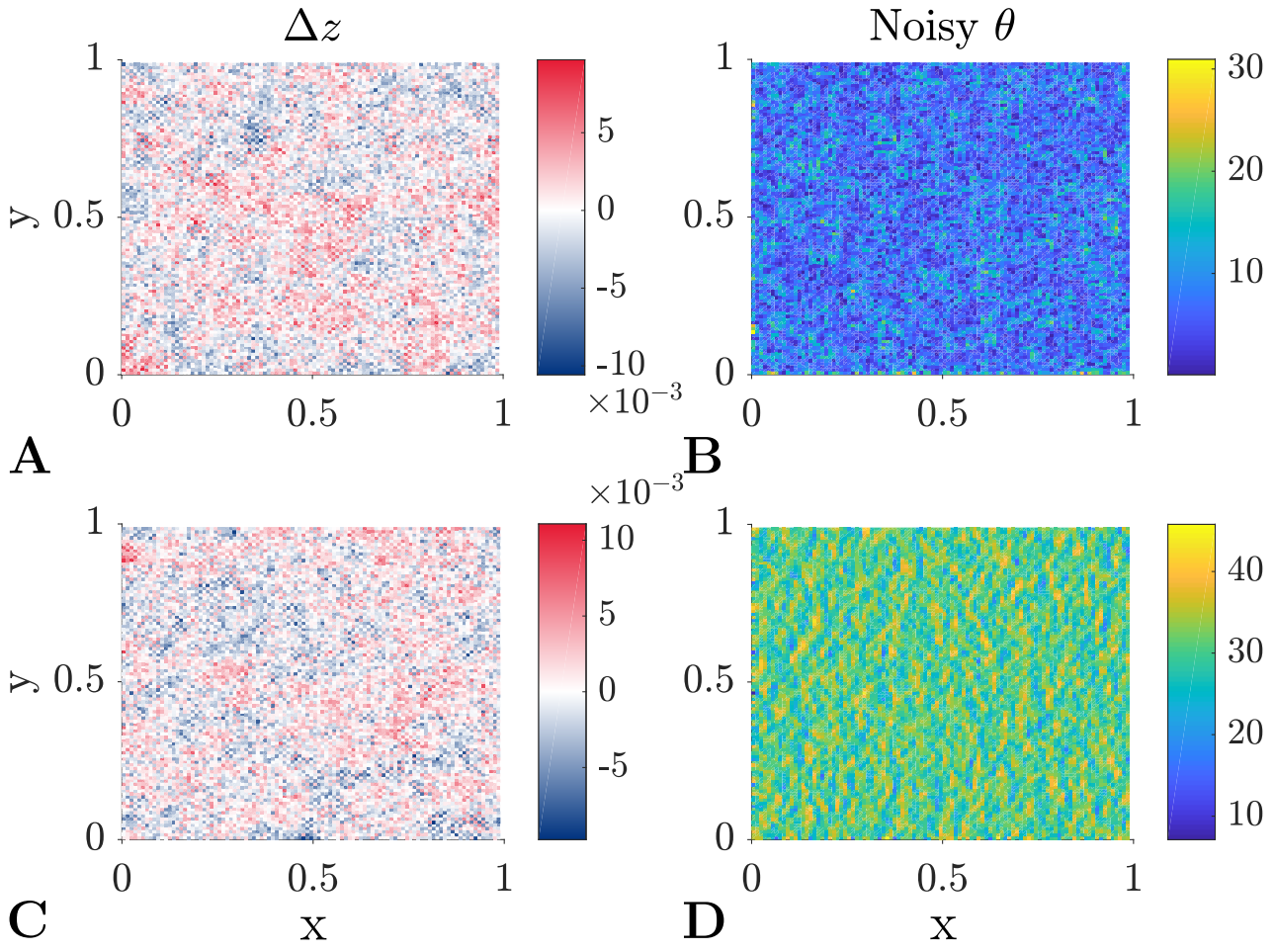

Figure 13: Vertical error distributions and slope calculations assuming an autoregressive law with a contiguity weight matrix as defined in equation 8, yielding to spatial autocorrelation of errors as highlighted in A) and C). A) and B) are respectively synthetic DEM errors and slope values for a horizontal surface. C) and D) are the same results for a tilted surface with a slope of $\theta = 30°$. Positive errors in A) and C) are displayed in red, negative errors in blue.

C) or not (16A). This result is unsurprising as all calculations are made based on the dimensionless vertical error $\tilde{dz}$, and HiRISE has the highest $\tilde{dz}$ of all cameras. Other cameras display a maximum RMS ∼4 – 4.3° (CaSSIS, 16D, E and F), ∼3.5 – 3.9° (MOC, 16G, H and I) and ∼3.2 – 3.5° (HRSC, 16J, K and L), also for lowest input slopes θ. The global shape of the RMS versus θ law does not vary with cameras or definition of vertical errors: it always starts with a maximum for $\theta = 0°$, then RMS decreases until a flattening for low slope values around 4 to 20°, depending on the camera (HiRISE presents this flattening for slightly lower values than others). The RMS_{px} component (blue part of the histogram) of global RMS error also differs for HiRISE compared with other cameras. The RMS_{px}'s peak is shifted towards higher θ for HiRISE than other cameras for every law of errors: around $\theta = 20°$ instead of $\theta = 15°$. This yields to limited changes in RMS component ratio for the lowest θ, with the highest amount of RMS caused by RMS_Q. Surprisingly, the vertical error laws definition does not significantly change RMS values for every camera. We however notice that autoregressive errors modeled from the contiguity matrix imply slightly lower RMS values, typically around 5 – 10% lower. This effect is more visible in Figure 17 which summarizes RMS values for each camera and error laws within one plot, with HiRISE in 17A, CaSSIS in 17B, MOC in 17C and HRSC in 17D. The dashed line is RMS for the autoregressive errors with contiguity matrix. This law always shows the lowest RMS values for each camera. The solid and dotted lines are the results for independent errors and autoregressive errors with exponential matrix, respectively. Error bars are also displayed on this representation and remain small regarding RMS values.

4. Discussion

Our models are at least partially able to retrieve the distinctive slope patterns that occur on Mars steep slopes in the martian DEM. Hence, we interpret vertical errors as a pos-

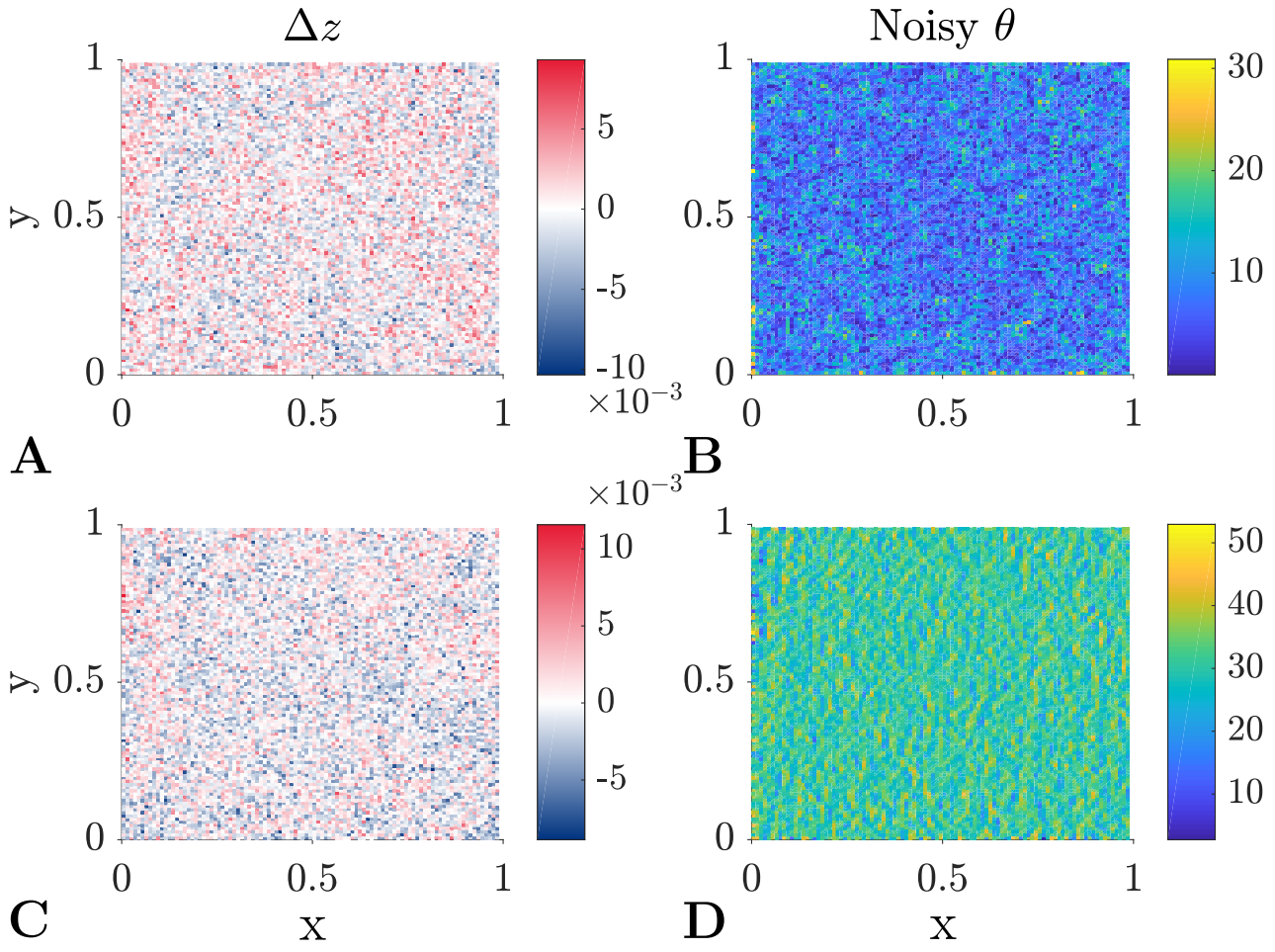

Figure 14: Same as Figure 13 with DEM vertical errors following an autoregressive law with an exponential weight matrix as defined in equation 9, yielding to spatial autocorrelation of errors as shown in A) and C).

sible source for patterns aligned normally to the slope direction. This interpretation is quite robust as patterns are present in slope maps for every law of vertical errors we model. Introducing more complex shapes such as craters and channel features highlight how slope patterns are stretched with respect to changing slope directions, which fits with our observations. Slope patterns found for noisy flat surfaces are therefore less convincing regarding the real slope patterns for CaSSIS data (figure 1E). Discrepancies can be explained by a mix of random vertical errors with small scale topographies of which dimensions are of the same order as the DEM spatial resolution, as small-scale features induce more variability in DEM elevations. Random noise has been invoked by previous studies to explain random patterns, for instance on HiRISE DEM elevations (Kirk et al., 2008). Also, smoothing filters improve the visual comparison between our synthetic and real DEMs. New studies need to focus on the impacts of various filters used in the making of such elevation data, in particular, they should assess how topography is affected by filtering process. In this study, we chose to provide laws for synthetic DEMs free of any filtering effect to provide general laws applicable to the widest range of DEMs.

By using synthetic DEMs, we manage to perform slope error calculations. The challenge is to evaluate our results against previous works on DEM quality assessment. Slope uncertainties have been studied within Kirk et al., 2003 for MOC using RMS estimations versus baseline through fast Fourier transform techniques, yielding RMS values between 1 – 3°, which is consistent with our estimations. Heipke et al., 2007 and Kirk et al., 2008 use the same method to find RMS values, with results of ∼5° for HRSC (with a 50 m baseline which corresponds to the spatial resolution we take for HRSC DEM from Gwinner et al., 2009) and ∼2° for HiRISE (at 1 m/pixel, Kirk et al., 2008). Our RMS values are lower on HRSC (around 1 – 2°) and higher on HiRISE (around 4 – 5°) than these previous results. Causes of such differences can be multiple: the dz parameter we define (table 1) varies with DEM and as we show it, slight variations of dz induces substantial changes in slopes and by extension in RMS values. Potential sources of errors from the DEM are multiple (e.g. Fisher and Tate, 2006, we take the example of a DEM produced by stereophotogrammetry to illustrate this

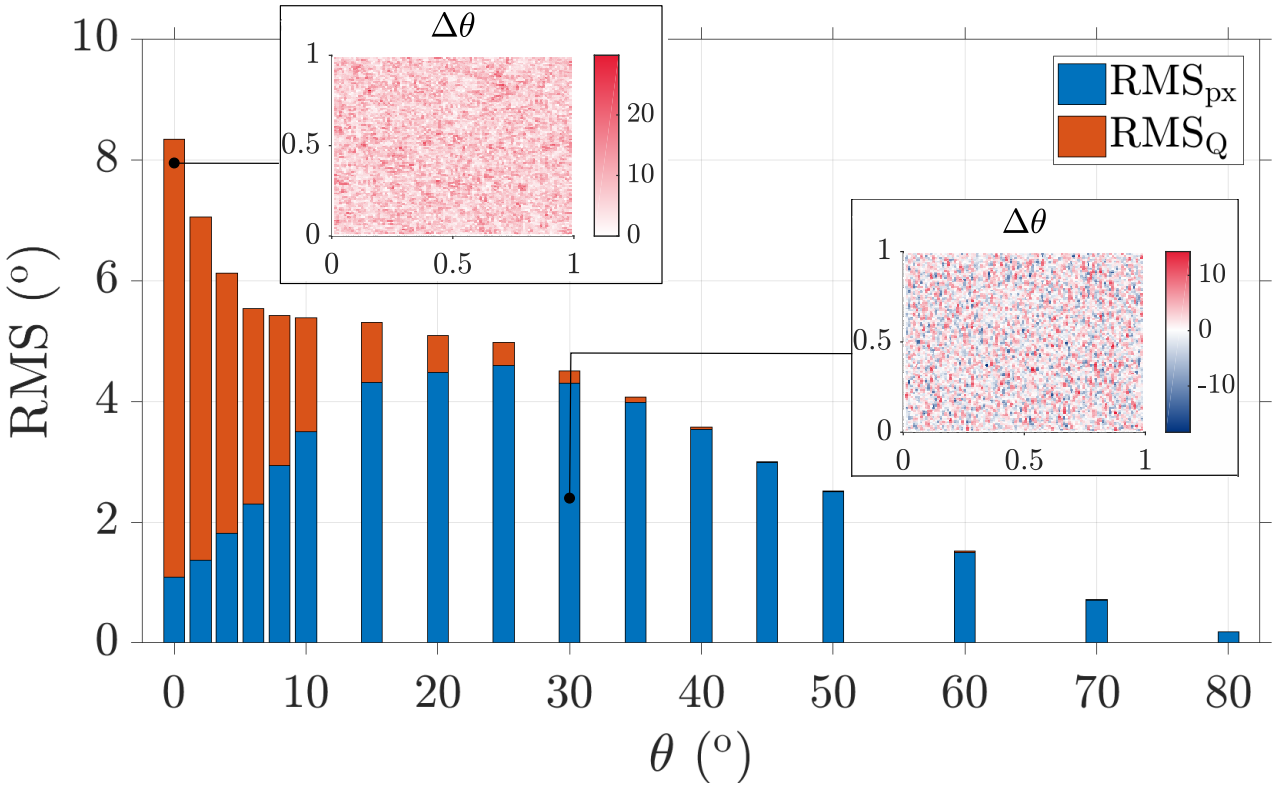

Figure 15: Cumulative histogram including RMS_Q (in orange) and RMS_{px} (in blue) with HiRISE parameters, with emphasis put on slope differences pattern at initial slopes $\theta = 0°$ and 30°.

idea for the next development): stereocorrelation between two images as well as interpolation methods or triangulation steps are all affected by the stereopipeline used in the making of a DEM. ASP (Ames Stereo Pipeline, Beyer et al., 2018), SOCET SET (®BAE Systems, used in HiRISE team's DEM, Kirk et al., 2008) or 3DPD (CaSSIS DEM, Re et al., 2019) are examples of stereopipelines applied in DEM production on Mars. ASP and SOCET SET stereopipeline results have been investigated on a HiRISE DEM by Tebolt et al., 2020. Authors present how slope calculations can yield varying spatial textures depending on the stereopipeline used to create the HiRISE DEM (ASP or SOCET SET). The standard deviation of the slope distribution is also visually different (Tebolt et al., 2020, their Figure 13). Thus, even if global structure of stereopipelines remain comparable, more specific procedures to remove jitters or filters applied to images within the stereopipelines differ. Also, we must take into account that camera parameters are different as well as the chosen method to create DEM (stereophotogrammetry, LiDAR, photoclinometry are three examples). Such differences lead to some complexities in the determination of DEM errors for each DEM created. This assumes first order spatially random errors on synthetic DEM are the more acceptable choice regarding all variables for the production of DEM data.

We define vertical errors as normally distributed, assuming that all corrections have been applied to remove spatially correlated errors in the DEM. We can argue this from a purely theoretical point of view, as errors are both typically the sum of systematic errors (constant shift or predictable shift, e.g. Eisenhart, 1963) and normally distributed errors (random noise, e.g. Ku et al., 1966). Considering real data, this definition is probably too simple and can be contested in the face of the number of possible sources of DEM errors leading to slope result variability(e.g. Fisher and Tate, 2006). This is the reason why we simulate the possible spatial correlation of errors, in order to understand the impact of similar errors in neighboring pixels. The source of correlated errors can be linked to how DEMs are created. For instance, the stereophotogrammetry method performs a stereocorrelation process between two images. That is then used to create disparity maps, which contain the offsets between what have been interpreted as corresponding pixels between the two images. However, the quality of the disparity map is not constant due to varying illumination conditions of some areas or low contrast regions in shadows or homogeneous surfaces. These uncertainties can lead to errors in pixels matching. Matching error is more common in steep terrains due to the lack of image contrast induced by shadowing. This is why there are interpolated areas within HiRISE DEM (Kirk et al., 2008) or lower stereo correlation quality parts on CaSSIS DEM (Re et al., 2019). Thus, it seems that spatial correlation of errors arises from stereocorrelation.

The choice of computing slopes on synthetic DEMs needs also to be discussed. One of the main differences comes from our knowledge of the "true" surface. For a synthetic DEM, we have perfect knowledge of the surface as we model them

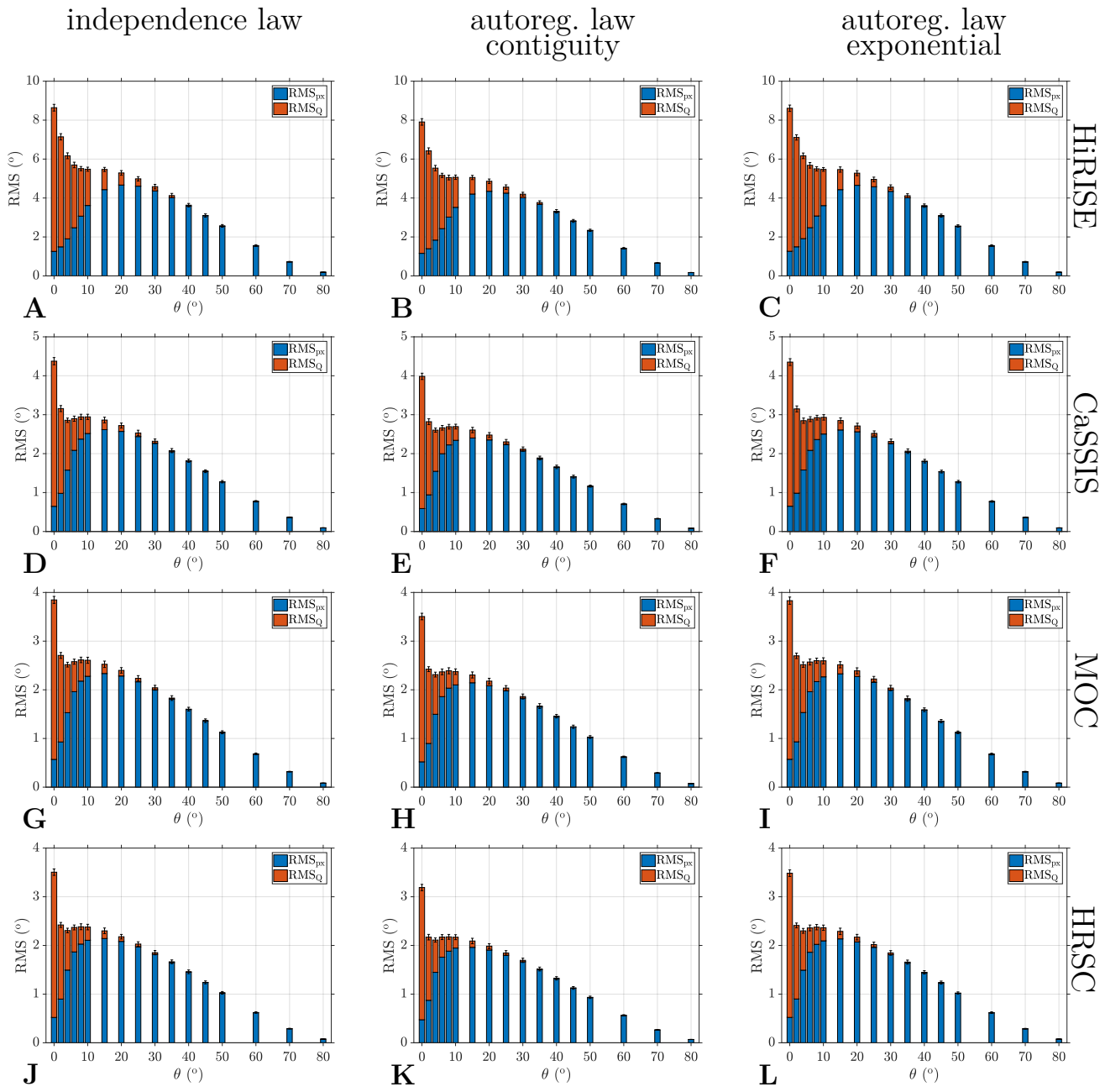

Figure 16: RMS values for different sets of parameters to model martian cameras. Each component of RMS is described under the form of a cumulative histogram, with RMS_Q (in orange) and RMS_{px} (in blue). A) B) and C) are cumulative histograms assuming an independence law, an autoregressive law with a contiguity weight matrix and an autoregressive law with an exponential weight matrix, respectively, for HiRISE parameters. The same structure is followed in D), E), F) for CaSSIS parameters, G), H), I) for MOC parameters and J), K), L) for HRSC parameters.

as a true surface. The vertical elevation has the highest precision available, as the DEM surface is defined from an analytical function, so precision is only limited by the computer error on the numbers, which is very small. The introduction of vertical errors is well known, and providing constraints on the way vertical errors are propagated to slopes is quite straightforward. The main issue is to find the best statistical descriptors of slope errors distribution. For real DEM data, elevation values are the combination of the real surface and vertical errors. It is difficult, if not impossible, to extract DEM vertical errors at pixel scale as they are included in the estimation of standard deviations (e.g. Stillman et al., 2020)

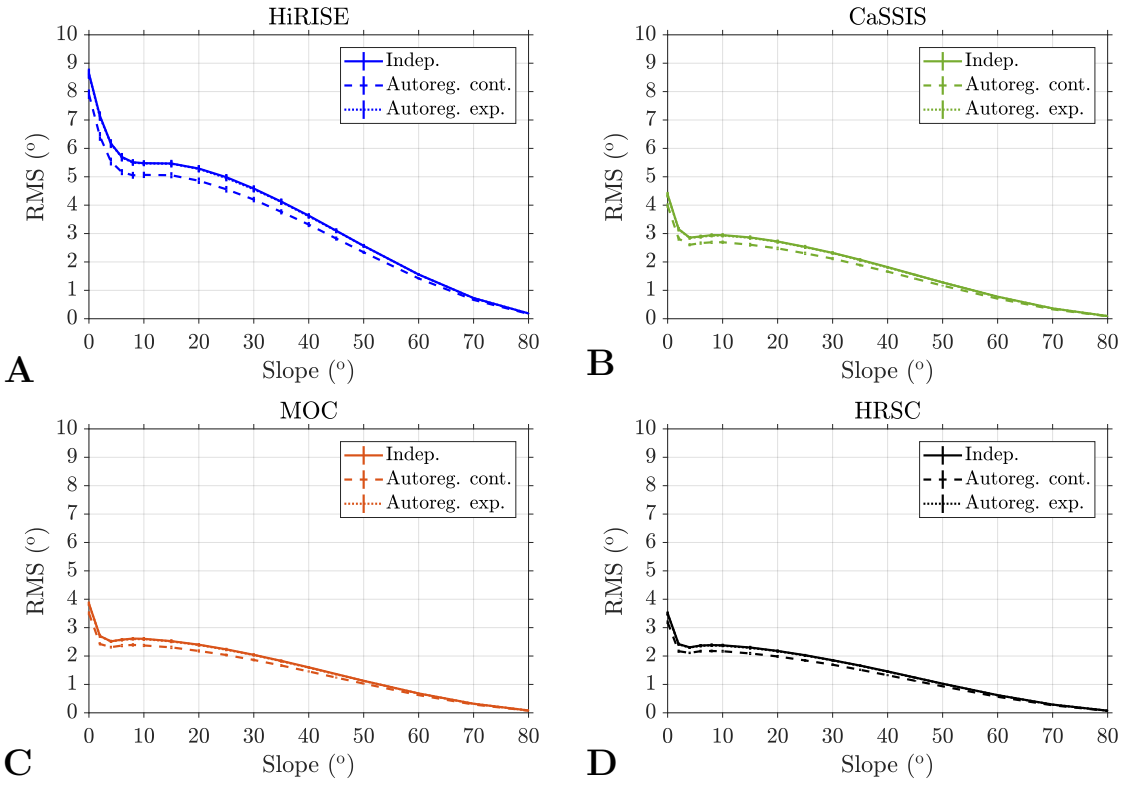

Figure 17: RMS values as a function of the input slope for each camera's parameters. Four slope errors laws are represented for A) HiRISE, B) CaSSIS, C) MOC and D) HRSC.

with the "true" topography.

Finally, we must emphasize that there are multiple methods to compute local slopes on a DEM. We choose to focus on the default method from commonly used GIS software (such as QGIS or ArcGIS), namely Horn's method (Horn, 1981), as it may be the favored method for geomorphological studies. Other slope computation methods using a similar technique of a 3×3 pixel moving window can result in significant local differences (Hodgson, 1995; Raaflaub and Collins, 2006; Tang et al., 2013). The discrepancies between methods for a given DEM are mainly dependent on the number of pixels used in the calculations of spatial derivatives ($\partial z/\partial x$ and $\partial z/\partial y$, equation 11): the fewer pixels that are included in the slope calculation, the higher the mean slope value (especially in steep slopes areas, Tang et al., 2013) and standard deviation value (Raaflaub and Collins, 2006) will be. Variations of mean slope values in steep terrains are in the order of a few degrees, but can reach ∼8° for a high resolution DEM between two different algorithms (Tang et al., 2013). Hence, the choice of method for computing local slope produces levels of variability comparable to the addition of random errors or autocorrelated errors. We thus recommend first a careful review of slope algorithms (see for instance Hodgson, 1995; Raaflaub and Collins, 2006; Skidmore, 1989; Tang et al., 2013) before their use in geomorphological studies, and secondly to keep in mind that the error laws presented in this study are only applicable to Horn's method. The alternative calculation methods may be studied following our protocol to provide new insights on how DEM vertical errors are propagated on slopes, including quantitative comparisons with the results from classical Horn's method.

5. Conclusion

We provide estimations of slope errors from a fully numerical method. We create synthetic DEMs of various geological terrains (craters with simple or complex shapes, channels, tilted or flat surface) and add vertical errors following constraints from previous studies on martian DEMs. After computing slope values from DEM data, we are able to discriminate the slope errors from the slope map in order to quantify them and build slope error laws. For tilted and noisy synthetic DEMs, we model slope error patterns displaying typical stretching perpendicular to the slope direction or random patterns on surfaces with low slopes, which is consistent with observations on slope values for real DEM data. Thus, we conclude that these slope patterns are caused by DEM vertical errors, which can be spatially autocorrelated or not. Slope error estimations have been calculated using RMS components following the definition from Pontius et al., 2008 for sets of parameters modeling four martian cameras: HiRISE, CaSSIS, MOC and HRSC. We find that for the same DEM vertical error distribution, the highest re-

sulting slope errors are restricted to low slope values. The highest slope variability is instead included within mid slope values, from around 10 to 40°. We recommend the use of the laws presented in this work as a first estimation of slope errors. We advise considering these new laws jointly with the careful examination of previous studies in order to evaluate slope uncertainties in topography studies. From this initial work, further development would seek to include alternative ways to compute slopes, to quantify how different each of the slope algorithms are and how they propagate vertical errors to slope errors. We can also imagine different shapes for synthetic models, especially including high frequency variability in topography through the addition of boulders, or modelling other vertical error distributions to obtain a more complete understanding of DEM slope errors. Finally, as the effect smoothing filters have on the production of DEMs remains poorly understood; some substantial work still needs to be done to provide useful and practical tools to facilite future study of topographic data by the planetary sciences community.

Declaration of Competing interest

None.

Acknowledgements

The authors would like to thank two anonymous reviewers for their careful reviews which significantly improve the quality of this manuscript. Cathy Quantin-Nataf has been supported by the Agence Nationale de la Recherche (ANR, ANR-18-ERC1-0005). We would like to thank E. Simioni and C. Re, from the Osservatorio Astronomico di Padova (OAPD), part of the Istituto Nazionale di Astrofisica (INAF), for providing the CaSSIS DTM used in this work. We also thank Mike Tetley for the English corrections that greatly contributed to the overall readability of this manuscript.

References

Acton, C.H., 1996. Ancillary data services of nasa's navigation and ancillary information facility. Planetary and Space Science 44, 65–70.

Ansan, V., Mangold, N., 2013. 3d morphometry of valley networks on mars from hrsc/mex dems: Implications for climatic evolution through time. Journal of Geophysical Research: Planets 118, 1873–1894.

Baker, V.R., Kochel, R.C., 1978. Morphometry of streamlined forms in terrestrial and martian channels, in: Lunar and Planetary Science Conference Proceedings, pp. 3193–3203.

Beyer, R.A., Alexandrov, O., McMichael, S., 2018. The ames stereo pipeline: Nasa's open source software for deriving and processing terrain data. Earth and Space Science 5, 537–548. doi:https://doi.org/10.1029/2018EA000409.

Chojnacki, M., McEwen, A., Dundas, C., Ojha, L., Urso, A., Sutton, S., 2016. Geologic context of recurring slope lineae in melas and coprates chasmata, mars. Journal of Geophysical Research: Planets 121, 1204–1231.

Craddock, R.A., Maxwell, T.A., Howard, A.D., 1997. Crater morphometry and modification in the sinus sabaeus and margaritifer sinus regions of mars. Journal of Geophysical Research: Planets 102, 13321–13340.

Dundas, C.M., McEwen, A.S., Chojnacki, M., Milazzo, M.P., Byrne, S., McElwaine, J.N., Urso, A., 2017. Granular flows at recurring slope lineae on mars indicate a limited role for liquid water. Nature geoscience 10, 903.

Dunn, M., Hickey, R., 1998. The effect of slope algorithms on slope estimates within a gis. Cartography 27, 9–15. doi:10.1080/00690805.1998.9714086.

Eisenhart, C., 1963. Realistic evaluation of the precision and accuracy of instrument calibration systems. Journal of Research of the National Bureau of Standards 67C.

Fisher, P.F., Tate, N.J., 2006. Causes and consequences of error in digital elevation models. Progress in physical Geography 30, 467–489. doi:10.1191/0309133306pp492ra.

Gwinner, K., Scholten, F., Spiegel, M., Schmidt, R., Giese, B., Oberst, J., Heipke, C., Jaumann, R., Neukum, G., 2009. Derivation and validation of high-resolution digital terrain models from mars express hrsc data. Photogrammetric Engineering & Remote Sensing 75, 1127–1142. doi:https://doi.org/10.14358/PERS.75.9.1127.

Heipke, C., Oberst, J., Albertz, J., Attwenger, M., Dorninger, P., Dorrer, E., Ewe, M., Gehrke, S., Gwinner, K., Hirschmüller, H., Kim, J., Kirk, R., Mayer, H., Muller, J.P., Rengarajan, R., Rentsch, M., Schmidt, R., Scholten, F., Shan, J., Spiegel, M., Wählisch, M., Neukum, G., 2007. Evaluating planetary digital terrain models—the hrsc dtm test. Planetary and Space Science 55, 2173–2191. doi:https://doi.org/10.1016/j.pss.2007.07.006.

Heuvelink, G.B.M., Burrough, P.A., Stein, A., 1989. Propagation of errors in spatial modelling with gis. International Journal of Geographical Information Systems 3, 303–322. doi:10.1080/02693798908941518.

Hodgson, M.E., 1995. What gell size does the gomputed slope/aspect angle reptesent? Photogrammetric Engineering & Remote Sensing 6, 513–517.

Horn, B.K.P., 1981. Hill shading and the reflectance map. Proceedings of the IEEE 69, 14–47. doi:10.1109/PROC.1981.11918.

Hunter, G.J., Goodchild, M.F., 1997. Modeling the uncertainty of slope and aspect estimates derived from spatial databases. Geographical Analysis 29, 35–49. doi:https://doi.org/10.1111/j.1538-4632.1997.tb00944.x.

Jaumann, R., Neukum, G., Behnke, T., Duxbury, T., Eichentopf, K., Flohrer, J., Gasselt, S., Giese, B., Gwinner, K., Hauber, E., Hoffmann, H., Hoffmeister, A., Köhler, U., Matz, K.D., McCord, T., Mertens, V., Oberst, J., Pischel, R., Reiss, D., Ress, E., Roatsch, T., Saiger, P., Scholten, F., Schwarz, G., Stephan, K., Wählisch, M., 2007. The high-resolution stereo camera (hrsc) experiment on mars express: Instrument aspects and experiment conduct from interplanetary cruise through the nominal mission. Planetary and Space Science 55, 928 – 952. URL: http://www.sciencedirect.com/science/article/pii/S0032063306003448, doi:https://doi.org/10.1016/j.pss.2006.12.003.

Kirk, R., Howington-Kraus, E., Rosiek, M., Anderson, J., Archinal, B., Becker, K., Cook, D., Galuszka, D., Geissler, P., Hare, T., et al., 2008. Ultrahigh resolution topographic mapping of mars with mro hirise stereo images: Meter-scale slopes of candidate phoenix landing sites. Journal of Geophysical Research: Planets 113.

Kirk, R.L., Howington-Kraus, E., Redding, B., Galuszka, D., Hare, T.M., Archinal, B.A., Soderblom, L.A., Barrett, J.M., 2003. High-resolution topomapping of candidate mer landing sites with mars orbiter camera narrow-angle images. Journal of Geophysical Research: Planets 108.

Ku, H.H., et al., 1966. Notes on the use of propagation of error formulas. Journal of Research of the National Bureau of Standards 70, 263–273.

Le Gallo, J., 2000. Econométrie spatiale (1, Autocorrélation spatiale). Research Report. Laboratoire d'analyse et de techniques économiques(LATEC). URL: https://hal.archives-ouvertes.fr/hal-01527290.

Malin, M.C., Edgett, K.S., 2000. Evidence for recent groundwater seepage and surface runoff on mars. Science 288, 2330–2335.

McEwen, A.S., Eliason, E.M., Bergstrom, J.W., Bridges, N.T., Hansen, C.J., Delamere, W.A., Grant, J.A., Gulick, V.C., Herkenhoff, K.E., Keszthelyi, L., et al., 2007. Mars reconnaissance orbiter's high resolution imaging science experiment (hirise). Journal of Geophysical Research: Planets 112.

McEwen, A.S., Ojha, L., Dundas, C.M., Mattson, S.S., Byrne, S., Wray, J.J., Cull, S.C., Murchie, S.L., Thomas, N., Gulick, V.C., 2011. Seasonal

flows on warm martian slopes. Science 333, 740–743.

McMillen, D.P., 1992. Probit with spatial autocorrelation. Journal of Regional Science 32, 335–348. doi:https://doi.org/10.1111/j.1467-9787.1992.tb00190.x.

Melosh, H.J., 1989. Impact cratering: A geologic process. volume 11.

Millot, C., Quantin-Nataf, C., Leyrat, C., Enjolras, M., 2021. Local topography effects on the surface temperatures on mars–application to the case of recurring slope lineae (rsl). Icarus , 114136doi:https://doi.org/10.1016/j.icarus.2020.114136.

Neukum, G., Jaumann, R., 2004. Hrsc: The high resolution stereo camera of mars express, in: Mars Express: The Scientific Payload, pp. 17–35.

Pontius, R.G., Thontteh, O., Chen, H., 2008. Components of information for multiple resolution comparison between maps that share a real variable. Environmental and Ecological Statistics 15, 111–142.

Quantin-Nataf, C., Carter, J., Mandon, L., Thollot, P., Balme, M., Volat, M., Pan, L., Loizeau, D., Millot, C., Breton, S., Dehouck, E., Fawdon, P., Gupta, S., Davis, J., Grindrod, P.M., Pacifici, A., Bultel, B., Allemand, P., Ody, A., Lozach, L., Broyer, J., 2021. Oxia planum: The landing site for the exomars "rosalind franklin" rover mission: Geological context and prelanding interpretation. Astrobiology 0, null. URL: https://doi.org/10.1089/ast.2019.2191, doi:10.1089/ast.2019.2191, arXiv:https://doi.org/10.1089/ast.2019.2191. pMID: 33400892.

Raaflaub, L.D., Collins, M.J., 2006. The effect of error in gridded digital elevation models on the estimation of topographic parameters. Environmental Modelling & Software 21, 710–732. doi:https://doi.org/10.1016/j.envsoft.2005.02.003.

Re, C., Tulyakov, S., Simioni, E., Mudric, T., Cremonese, G., Thomas, N., 2019. Performance evaluation of 3dpd, the photogrammetric pipeline for the cassis stereo images. ISPRS - International Archives of the Photogrammetry, Remote Sensing and Spatial Information Sciences XLII-2/W13, 1443–1449. URL: https://www.int-arch-photogramm-remote-sens-spatial-inf-sci.net/XLII-2-W13/1443/2019/, doi:10.5194/isprs-archives-XLII-2-W13-1443-2019.

Robbins, S.J., Hynek, B.M., 2012. A new global database of mars impact craters > 1 km: 2. global crater properties and regional variations of the simple-to-complex transition diameter. Journal of Geophysical Research: Planets 117.

Schmidt, F., Andrieu, F., Costard, F., Kocifaj, M., Meresescu, A.G., 2017. Formation of recurring slope lineae on mars by rarefied gas-triggered granular flows. Nature Geoscience 10, 270–273.

Simioni, E., Re, C., Mudric, T., Pommerol, A., Thomas, N., 2017. A photogrammetric pipeline for the 3d reconstruction of cassis images on board exomars tgo. The International Archives of Photogrammetry, Remote Sensing and Spatial Information Sciences 42, 133–139. doi:10.5194/isprs-archives-XLII-3-W1-133-2017.

Skidmore, A.K., 1989. A comparison of techniques for calculating gradient and aspect from a gridded digital elevation model. International Journal of Geographical Information Systems 3, 323–334. doi:10.1080/02693798908941519.

Smith, D.E., Zuber, M.T., Solomon, S.C., Phillips, R.J., Head, J.W., Garvin, J.B., Banerdt, W.B., Muhleman, D.O., Pettengill, G.H., Neumann, G.A., et al., 1999. The global topography of mars and implications for surface evolution. Science 284, 1495–1503.

Stillman, D.E., Bue, B.D., Wagstaff, K.L., Primm, K.M., Michaels, T.I., Grimm, R.E., 2020. Evaluation of wet and dry recurring slope lineae (rsl) formation mechanisms based on quantitative mapping of rsl in garni crater, valles marineris, mars. Icarus 335, 113420. doi:10.1016/j.icarus.2019.113420.

Sutton, S., Chojnacki, M., Kilgallon, A., Team, H., 2015. Precision and accuracy of simultaneously collected hirise digital terrain models, in: 46th Lunar and Planetary Science Conference, Lunar and Planetary Institute, Houston. p. Abstract #3010. URL: http://www.lpi.usra.edu/meetings/lpsc2015/pdf/3010.pdf.

Sutton, S.S., Chojnacki, M., McEwen, A.S., Kirk, R.L., Dundas, C.M., Schaefer, E.I., Conway, S.J., Diniega, S., Portyankina, G., Landis, M.E., et al., 2022. Revealing active mars with hirise digital terrain models. Remote Sensing 14, 2403. URL: https://www.mdpi.com/2072-4292/14/10/2403.

Tang, J., Pilesjö, P., Persson, A., 2013. Estimating slope from raster data–a test of eight algorithms at different resolutions in flat and steep terrain. Geodesy and Cartography 39, 41–52. doi:https://doi.org/10.3846/20296991.2013.806702.

Taylor, J., 1997. Introduction to error analysis, the study of uncertainties in physical measurements.

Tebolt, M., Levy, J., Goudge, T., Schorghofer, N., 2020. Slope, elevation, and thermal inertia trends of martian recurring slope lineae initiation and termination points: Multiple possible processes occurring on coarse, sandy slopes. Icarus 338, 113536. URL: http://www.sciencedirect.com/science/article/pii/S0019103519305779, doi:https://doi.org/10.1016/j.icarus.2019.113536.

Thomas, N., Cremonese, G., Ziethe, R., Gerber, M., Brändli, M., Bruno, G., Erismann, M., Gambicorti, L., Gerber, T., Ghose, K., et al., 2017. The colour and stereo surface imaging system (cassis) for the exomars trace gas orbiter. Space science reviews 212, 1897–1944. doi:https://doi.org/10.1007/s11214-017-0421-1.

Watters, W.A., Geiger, L.M., Fendrock, M., Gibson, R., 2015. Morphometry of small recent impact craters on mars: Size and terrain dependence, short-term modification. Journal of Geophysical Research: Planets 120, 226–254.

Williams, R.M., Phillips, R.J., 2001. Morphometric measurements of martian valley networks from mars orbiter laser altimeter (mola) data. Journal of Geophysical Research: Planets 106, 23737–23751.

Wood, C.A., 1973. Moon: Central peak heights and crater origins. Icarus 20, 503–506. doi:https://doi.org/10.1016/0019-1035(73)90023-7.

Zuber, M.T., Smith, D., Solomon, S., Muhleman, D., Head, J., Garvin, J., Abshire, J., Bufton, J., 1992. The mars observer laser altimeter investigation. Journal of Geophysical Research: Planets 97, 7781–7797.